
This is an electronic reprint of the original article.
This reprint may differ from the original in pagination and typographic detail.

Kronberg, Rasmus; Laasonen, Kari

Reconciling the Experimental and Computational Hydrogen Evolution Activities of Pt(111) through DFT-Based Constrained MD Simulations

Published in:
ACS Catalysis

DOI:
[10.1021/acscatal.1c00538](https://doi.org/10.1021/acscatal.1c00538)

Published: 02/07/2021

Document Version
Publisher's PDF, also known as Version of record

Published under the following license:
CC BY

Please cite the original version:
Kronberg, R., & Laasonen, K. (2021). Reconciling the Experimental and Computational Hydrogen Evolution Activities of Pt(111) through DFT-Based Constrained MD Simulations. *ACS Catalysis*, 11(13), 8062-8078. <https://doi.org/10.1021/acscatal.1c00538>

This material is protected by copyright and other intellectual property rights, and duplication or sale of all or part of any of the repository collections is not permitted, except that material may be duplicated by you for your research use or educational purposes in electronic or print form. You must obtain permission for any other use. Electronic or print copies may not be offered, whether for sale or otherwise to anyone who is not an authorised user.

Reconciling the Experimental and Computational Hydrogen Evolution Activities of Pt(111) through DFT-Based Constrained MD Simulations

Rasmus Kronberg and Kari Laasonen*



Cite This: *ACS Catal.* 2021, 11, 8062–8078



Read Online

ACCESS |



Metrics & More



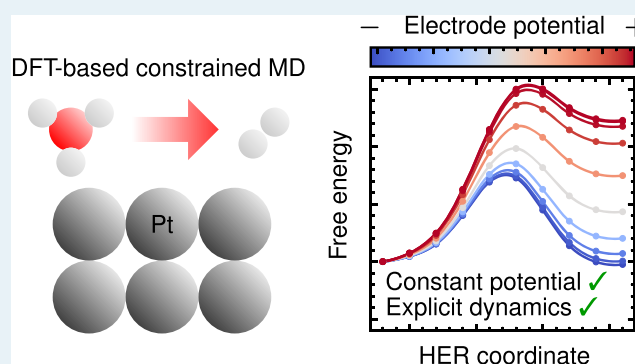
Article Recommendations



Supporting Information

ABSTRACT: The computational hydrogen evolution activity of Pt(111) remains controversial due to apparent discrepancies with experiments concerning rate-determining activation free energies and equilibrium hydrogen coverages. A fundamental source of error may lie within the static representations of the metal–water interface commonly employed in density functional theory (DFT)-based kinetic models neglecting important entropic effects on reaction dynamics. In this work, we present a dynamic reassessment of the Volmer–Tafel hydrogen evolution pathway on Pt(111) through DFT-based constrained molecular dynamics simulations and thermodynamic integration. Hydrogen coverage effects are gauged at two distinct surface saturations, while the critical potential dependence and constant potential conditions are accounted for using a capacitive model of the electrified interface. The uncertainty in the highly nontrivial treatment of the electrode potential is carefully examined, and we provide a quantitative estimation of the error associated with dynamically simulated electrochemical barriers. The dynamic description of the electrochemical interface promotes a substantial decrease of the Tafel free energy barrier as the coverage is increased to a full monolayer. This follows from a decreased entropic barrier due to suppressed adlayer dynamics compared to the unsaturated surface, a detail easily missed by static calculations predicting notably higher barriers at the same coverage. Due to observed endergonic adsorption of active hydrogen intermediates, the Tafel step remains rate-determining irrespective of the coverage as illustrated by composed Volmer–Tafel free energy landscapes. Importantly, our explicitly dynamic approach avoids the ambiguous choice of frozen solvent configuration, decreasing the reliance on error cancellation and paving the way for less biased electrochemical simulations.

KEYWORDS: hydrogen evolution, Pt(111), DFT, constrained MD, thermodynamic integration, electrode potential, electrochemical barriers



1. INTRODUCTION

Rational design of cost-effective electrocatalysts is required for promoting a sustainable deployment of renewable electrochemical energy technologies such as electrolyzers and fuel cells that drive the interconversion of electrical and chemical energy via the redox reactions of hydrogen and oxygen.¹ For this purpose, computational research is conducted widely to access atomistic information on structure and activity that experiments alone struggle to resolve. Although density functional theory (DFT) constitutes by far the most applied computational methodology, different schools and modeling paradigms regarding the way in which DFT models are applied exist.^{2,3}

Fast, descriptor-oriented materials screening relies on simple structural and nongeometric variables, e.g. (generalized) coordination numbers,⁴ adsorption energies⁵ and metal d-band moments⁶ using which approximate activity trends within an ensemble of catalyst candidates are inferred applying

conceptual tools such as the Sabatier principle. Recently, machine learning has also emerged as an intriguing method by means of which even further accelerated materials discovery is projected.^{7–9} Conversely, more accurate information on catalytic performance can be obtained via explicit kinetic modeling wherein the actual transition paths of examined reactions are optimized to estimate heights of rate-determining activation barriers.^{10–14} This alternative is evidently more rigorous considering that the experimentally relevant reaction

Received: February 4, 2021

Revised: May 13, 2021

conditions are typically accounted for as precisely as possible, but comes naturally at an increased computational expense.

Within the framework of kinetic modeling, several algorithms for optimizing transition paths have been developed, of which perhaps the most applied is the nudged elastic band (NEB) method.^{15,16} Although being widely used also for electrochemical reactions, the NEB method is inherently a static minimum energy path (MEP) optimization algorithm requiring well-defined initial and final states as input for reliable performance. This is problematic as most electrochemical reactions of interest occur at dynamic electrode–electrolyte interfaces where finite-temperature solvent fluctuations indisputably affect the geometries and energetics of states along a transition path.² Consequently, the solvent degrees of freedom play a decisive part in the reaction coordinate, thereby constituting an important entropic contribution to e.g. reaction barriers.^{14,17} Moreover, the fluctuating interfacial solvent and formation of the electrochemical double-layer (EDL) structure require considerable statistical sampling over extended simulation times to appropriately represent the microscopic details of the electrified solid–liquid interface.^{18,19}

Platinum constitutes arguably the best performing electrode material for several electrocatalyzed reactions, including the hydrogen evolution reaction (HER), i.e. the cathodic half-reaction of electrochemical water splitting. In addition to its catalytic efficiency, the well-defined and stable structure of close-packed crystal facets have established low-index platinum as an experimentally relevant prototype system for fundamental studies of electrochemical interfaces and reactions catalyzed thereon.^{11–13,18–25} Despite the great desire to develop electrocatalysts free of critical platinum group metals, applied computational methods are ideally first benchmarked against such well-known systems to establish the level of theory necessary for experimentally meaningful and precise predictions. Indeed, the observed reaction rates on more complex catalyst materials correspond to macroscopic averages originating from diverse moieties the local activities of which are challenging to decouple and characterize. This naturally limits the amount of available reference data for systems more novel and intricate than the quintessential close-packed platinum electrode.

However, even for seemingly simple processes such as HER on Pt(111), notable discrepancies exist between the computationally and experimentally observed activities. Specifically, the pioneering DFT simulations of HER on Pt(111)^{11,26} proposed substantial barriers of up to 0.85 eV for the rate-determining elementary step (RDS) at the thermodynamic equilibrium potential, whereas experimental studies^{27,28} have in contrast suggested considerably lower apparent activation energies, even as low as 0.2 eV. This disparity translates to an immense activity difference due to the exponential dependence of reaction rates on activation energies. We note, however, that a direct comparison of experimental activation energies and computational barriers is strictly speaking ill-defined as the apparent experimental barriers correspond to the enthalpic part of the activation *free* energy as obtained by measuring the temperature dependence of the HER and applying Arrhenius' rate formalism.²⁹ Conversely, barriers from DFT minimum energy path calculations only reflect ground state electronic energy changes. Thus, observed discrepancies can be partially ascribed to lacking zero-point energy contributions when comparing computational barriers from static MEP calcula-

tions to experimental activation energies. On the other hand, the entropic contribution missing from the apparent activation energy complicates a direct comparison of experiments against dynamically simulated free energy barriers.

Nonetheless, early computational studies as well as other more recent efforts to simulate HER on platinum^{12,13} have applied frozen water bilayer or cluster representations of the aqueous environment in conjunction with and as imposed by the static NEB method. The origin of the ice-like solvent models can be motivated based on early experiments aiming at characterizing the metal–water interface at ultrahigh vacuum (UHV) conditions. These measurements suggested that the first solvent contact layer adopts a stationary structure composed of water hexamers with maximized surface–water and water–water interactions.^{30,31} Recent experiments and simulations have, however, largely disproven this model by demonstrating that on several metallic surfaces the interface is more diverse and disordered, exhibiting structurally more complex motifs and, most importantly, considerable solvent fluctuations.^{19,23} Consequently, a reassessment of the computational hydrogen evolution activity of Pt(111) considering the significance of explicit interfacial dynamics is highly warranted. A dynamic simulation of the HER would importantly allow the estimation of the activation free energy including entropic contributions as previously argued necessary to properly comprehend the HER on Pt(111).²⁹ Any remaining differences between the experimental activation enthalpy and the simulated free energy would be naturally ascribed to entropic effects.

To this end, we present a thorough DFT investigation of the hydrogen evolution activity of single-crystal platinum based on constrained molecular dynamics (cMD) simulations and the thermodynamic integration method introduced by Sprik and Ciccotti.³² Specifically, we revisit the HER mechanism on Pt(111) according to the Volmer–Tafel pathway to resolve the influence of interfacial dynamics on the activation and reaction free energies. In addition to the interfacial dynamics, the surface coverage of strongly bound hydrogen as well as electrode potential effects are appropriately taken into account for a comprehensive treatise. Importantly, the uncertainty related to the treatment of the electrode potential is examined in detail and we provide to our knowledge the first quantitative estimation of the error associated with computational electrochemical barriers.

The remainder of this article is structured as follows. First, a thorough description of the applied theoretical and computational methods is given, including the details concerning the DFT-cMD simulations, the thermodynamic integration procedure and the employed reaction coordinates in [Section 2.1](#). Second, the theoretical aspects pertaining to constant potential corrections are outlined in [Section 2.2](#), followed by a description of the studied model systems and parameters of the electronic structure calculations in [Sections 2.3.1](#) and [2.3.2](#). The technical details of the dynamic and static reaction path simulations as well as the applied method for estimating electrode potential dependence are discussed in [Sections 2.3.3](#) and [2.3.4](#), respectively. The results of our work are then reported and evaluated, beginning with the simulated canonical Volmer–Tafel free energy profiles in [Section 3.1](#). The necessary treatment of the electrode potential dependence of the Volmer reaction is presented in [Section 3.2](#) and the uncertainties pertaining to the treatment of the electrode potential are quantified in the following [Section 3.2.1](#). A critical

discussion and comparison against previous experiments and computational works is presented in Section 3.3 and the main conclusions of our work are last summarized in Section 4.

2. THEORETICAL METHODS

2.1. Constrained Simulation of the Volmer–Tafel Mechanism. Rare events in dynamic environments, such as liquid phase chemical reactions, can be simulated by introducing a holonomic constraint $\sigma(\mathbf{q}) = \xi(\mathbf{q}) - \xi' = 0$ on a chosen reaction coordinate $\xi(\mathbf{q})$ along which the event under consideration is driven and sampling the system at different prescribed values ξ' of the coordinate.³² For an arbitrary number of constraints the Lagrangian of the unconstrained system \mathcal{L} is extended according to Equation 1

$$\mathcal{L}'(\mathbf{q}, \mathbf{p}) = \mathcal{L}(\mathbf{q}, \mathbf{p}) + \sum_i \lambda_i \sigma_i(\mathbf{q}) \quad (1)$$

where \mathbf{q} and \mathbf{p} are generalized positions and momenta and λ_i is the Lagrange multiplier enforcing the i th constraint $\sigma_i(\mathbf{q})$. The reaction coordinate $\xi(\mathbf{q})$ may correspond to a simple geometric parameter, such as a bond distance, or some more abstract quantity.^{33,34} Importantly, this reaction coordinate is generally not known *a priori* and a reasonable choice must be based on chemical intuition and monitored closely to ensure appropriate performance.

As the system is propagated subject to the defined constraint in an MD simulation, a biased statistical ensemble frequently referred to as the blue moon ensemble is sampled. The unbiased free energy profile associated with the rare event is obtained in accordance with Equation 2 by performing thermodynamic integration (TI) over the solvent averaged force $\langle f_s(\xi') \rangle_{\xi'}$, i.e. the bare force of constraint (Lagrange multiplier) corrected by a mass metric tensor as derived by Sprik and Ciccotti.³²

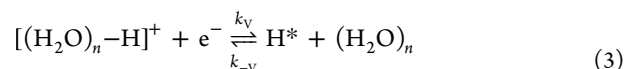
$$\Delta A(\xi) = - \int_{\xi_0}^{\xi} d\xi' \langle f_s(\xi') \rangle_{\xi'} \quad (2)$$

For simple reaction coordinates, such as functions of bond distances or generalized coordination numbers, corrections to the bare force of constraint are insignificant^{14,17,33} and the approximation $\langle f_s(\xi') \rangle_{\xi'} \approx \langle \lambda \rangle_{\xi'}$ is generally invoked.

The predominant HER reaction mechanism on Pt(111) remains a debated topic within the electrocatalysis community. While the Volmer–Tafel pathway, composed of a proton-coupled electron transfer (PCET) adsorption step followed by a purely chemical recombination of two adsorbed hydrogen intermediates, has been supported by several experimental and computational studies,^{11–13,28} the seminal work of Marković et al.²⁷ was unable to provide a definitive answer regarding the dominance of this mechanism. Although the alternative Heyrovský reaction has been computationally predicted to exhibit a reaction barrier several hundred meV larger than the Tafel step,^{11–13,26} this view has been lately questioned in light of new evidence.^{29,35,36} Notably, the barrier of the Heyrovský step has been argued to be overestimated by early computational studies following an incorrect referencing of energies to interfacial (pseudo initial state) protons instead of bulk ones.³⁵ Furthermore, it has been suggested that the Volmer–Tafel reaction could be operational only at small overpotentials and cathodically polarizing the electrode further would shift the dominant mechanism to the Volmer–Heyrovský pathway.³⁶ While we acknowledge that both HER mechanisms on Pt(111)

are possible and may even coexist, we choose to focus our present scope to the Volmer–Tafel pathway and demonstrate an advanced dynamic computational framework for modeling the reaction energetics of this mechanism. Although definitely interesting and desired, revisiting the Volmer–Heyrovský mechanism based on a rigorous dynamic modeling scheme as employed herein would constitute a topic for a research effort on its own.

Irrespective of the prevalent mechanism, the initial proton electroadsorption proceeds through the Volmer reaction in which a solvated proton $[(\text{H}_2\text{O})_n - \text{H}]^+$ adsorbs to the electrode surface according to



where k_V and k_{-V} are the rate constants of the forward and reverse reactions, respectively. While the subscripts $n = 1, 2$ and 4 in eq 3 correspond respectively to the hydronium (H_3O^+), Zundel (H_5O_2^+) and Eigen (H_9O_4^+) cations frequently used as models of aqueous hydronic species,³⁷ the relevant transition state through which hydrogen adsorption proceeds has been recently shown to involve an intermediate $n = 3$ complex (H_7O_3^+) in which the transferring proton is strongly oriented toward the electrode surface.¹⁴ The Volmer step is followed by the Tafel reaction where two adsorbed hydrogen intermediates H^* react to form molecular hydrogen H_2 ,



where k_T and k_{-T} are the rate constants of the forward and reverse reactions, respectively. Notably, the Tafel reaction is a purely chemical surface reaction involving only a minor amount of charge transfer required to compensate for desorption-induced changes in the surface dipole affecting the electrode potential.

Herein, we adopt a proton transfer coordinate for the Volmer reaction proposed and validated in our recent work.¹⁴ Namely, we consider the difference of bond distances between 1) the proton donating oxygen and the transferring proton and 2) the adsorption site (Pt top-site) and the transferring proton as defined by Equation 5,

$$\xi(\mathbf{r}) = |\mathbf{r}_\text{O} - \mathbf{r}_\text{H}| - |\mathbf{r}_\text{Pt} - \mathbf{r}_\text{H}| \quad (5)$$

For the Tafel reaction on the other hand a distance function is defined according to Equation 6, involving 1) the perpendicular distance between the centroids of the forming H_2 molecule and the Pt atoms constituting the outermost surface layer of the electrode and 2) the bond length between the recombining hydrogen atoms,

$$\xi(\mathbf{r}) = \hat{\mathbf{n}} \cdot \left(\frac{\mathbf{r}_\text{H} + \mathbf{r}'_\text{H}}{2} - \sum_{i \in \mathcal{S}} \frac{\mathbf{r}_{\text{Pt},i}}{N} \right) - |\mathbf{r}_\text{H} - \mathbf{r}'_\text{H}| \quad (6)$$

where \mathcal{S} denotes the set of N surface Pt atoms and $\hat{\mathbf{n}}$ is the unit normal of the surface. The labeling of atoms in Equations 5 and 6 is as defined in Figure 1.

As comprehensively elaborated in our previous work,¹⁴ distance difference-based reaction coordinates are flexible enough to allow the systems to explore the phase space and find a realistic transition path while still maintaining a sufficient degree of control over the reaction. Importantly, by avoiding direct constraints on bond lengths and surface separations,

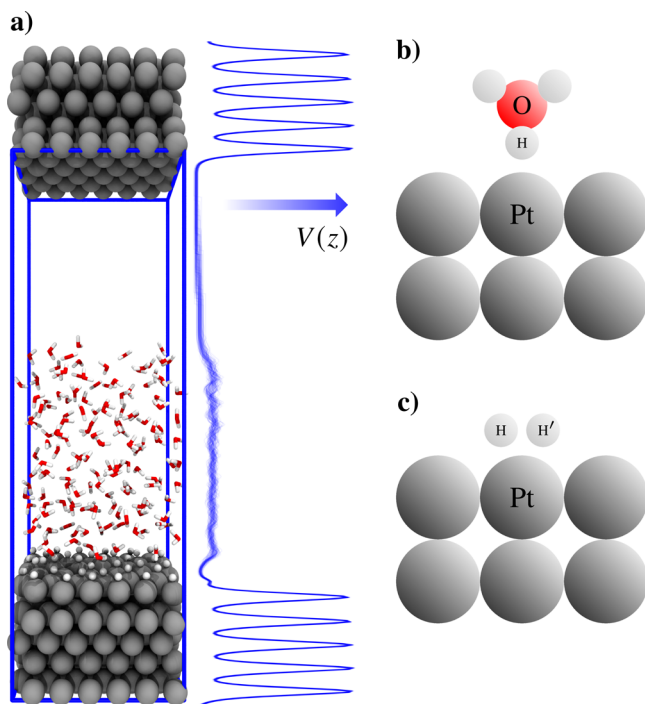


Figure 1. (a) Side-view of the simulated electrochemical interface with a 1 ML hydrogen coverage. Gray, red, and white spheres correspond to platinum, oxygen, and hydrogen atoms, respectively, and the blue box marks the boundaries of the simulation cell. The laterally averaged electrostatic potential $V(z)$ of the system is shown aligned next to the structural model. (b,c) Schematic illustration of the key species participating in (b) the Volmer reaction, i.e., the Pt surface and the adsorbing/desorbing solvated proton and (c) the Tafel reaction, i.e., the Pt surface and the associating/dissociating hydrogen atoms. The chemical symbols annotated in b and c are directly associated with the indices used in defining the respective reaction coordinates in eqs 5 and 6.

quenching of translational, rotational and vibrational degrees of freedom is avoided. Specifically, along the Volmer coordinate the Pt–H and H–O bonds are free to vibrate, while for the Tafel reaction translations in the xy -plane, rotations and vibrations of the H_2 molecule are possible. Moreover, the systems are free to decrease and/or increase whichever distance term is energetically more favorable depending on the progress of the reaction along the specified coordinate.

2.2. Constant Electrode Potential Models. Electrocatalyzed reactions involve charge transfer between the reacting species and the electrode. In conventional Kohn–Sham DFT simulations the total number of electrons in the system is fixed and the charge on the electrode must accordingly change upon charge transfer to or from the surface. As the electrode surface charge is intimately related to the electrostatic potential of the electrode, a critical issue arises—the electrode potential will change as the reaction progresses.³ Consequently, calculated quantities such as reaction energies and barriers are ill-defined from an electrochemical perspective as points along the reaction coordinate do not reflect constant potential conditions as enforced by a potentiostat in true electrochemical measurements. The grand canonical nature of electrochemistry in which the electrode is allowed to exchange electrons with an external bath in order to maintain a constant potential must necessarily be taken into account for obtaining consistent and

reliable results, either by means of approximate models^{11,26,38–42} or rigorously extended DFT formalisms.^{43,44} As the latter tend to be computationally prohibitive for large-scale systems of interest, more crude models are frequently adopted.

One of the first approximate approaches to a tunable electrode potential was introduced by the double reference method,^{38,39} which involves modeling an electrochemical reaction explicitly at different electrode charge states. In order to avoid a diverging electrostatic energy in the periodic simulations, a constant background charge is added and a 2-fold correction accounting for the changing electron count as well as the spurious interaction between the system and the homogeneous counter-charge is applied. The validity of the latter has, however, been questioned as the added charge is often delocalized on the electrode which conflicts with the assumptions underlying commonly applied correction terms initially developed for localized charged point defect calculations.⁴⁵

Another alternative is the size extrapolation method wherein the electrochemical reaction is investigated employing multiple simulation cells of increasing size.^{11,26} At the extrapolated limit of infinite lateral cell parameters the changing electron count on the electrode negligibly affects the electrostatic potential of the system, yielding converged values for the reaction barriers and energies. Controlling the electrode potential is often accomplished by varying the number of excess atoms (e.g., hydrogen, alkali metals or halogens) within the interfacial solvent that spontaneously ionize due to preferential electron transfer to or from the electrode. Although theoretically rather rigorous, the size extrapolation scheme unsurprisingly suffers from a considerable computational expense as multiple large-scale DFT simulations must be performed to appropriately capture the electrode potential dependence of electrochemical reactions. For a further discussion on the wide variety of constant electrode potential models, including implicit solvent-based methods invoking the modified Poisson–Boltzmann theory for the ionic counter-charge distribution, the reader is referred to the recent reviews on the subject.^{46,47}

For the sake of computational feasibility, a recent method introduced by Chan and Nørskov^{40,41} was applied in this work as an *a posteriori* grand canonical correction for the electrode potential dependence of the Volmer reaction. In this “charge extrapolation” method, the energy change along an electrochemical reaction path at constant potential conditions is assumed to consist of separable chemical and electrostatic contributions. While the chemical contribution is simply the energy difference between the compared states, the electrostatic contribution is approximated by treating the electrochemical interface and the charge transfer step as a discharging capacitor the energy of which depends on the potential as $E \sim qU \sim U^2$, where q is the stored charge and U the potential difference. In the absence of a strongly reorienting interfacial dipole, Chan and Nørskov derived Equation 7 for the energy difference between states μ and ν at the constant potential U_ν of the latter state,

$$\Delta\Omega_{\mu\nu}(U_\nu) = \underbrace{A_\mu(U_\mu) - A_\nu(U_\nu)}_{\text{chemical}} - \underbrace{\frac{(q_\mu - q_\nu)(U_\mu - U_\nu)}{2}}_{\text{electrostatic}} \quad (7)$$

where the symbol Ω is used to distinguish the constant potential corrected free energy from the canonical Helmholtz free energy A . Equation 7 applies equally well for both reaction

energies and barriers. Since each constraint along the reaction coordinate reflects a different average electrode potential U_μ and surface charge q_μ due to fractional electron transfer, constant potential free energy profiles are derived by referencing each constrained state μ to a single chosen reference ν along the reaction path. The electrode potential U_ν at this reference state sets the constant potential of the corrected free energy profile. By using each constrained trajectory in turn as a reference and setting the initial state free energies to zero, a set of corrected free energy profiles at different constant electrode potentials is obtained. This allows an efficient mapping of the electrode potential dependence of the key kinetic quantities.¹⁴ Importantly, while the charge extrapolation requires only a single reaction path simulation in contrast to the above briefly discussed methods, special attention should be given to the accurate calculation of the electrode potential and appropriate choice of charge partitioning scheme.

It is nonetheless noteworthy that electronically grand canonical calculations have witnessed substantial developments recently for example by the introduction of a fictitious potentiostat allowing simulated systems to exchange electrons with an external bath at fixed electrochemical potential.⁴⁸ Promisingly, some studies suggest that the slower charge dynamics and equilibration of the potential following a variation of the system electron count only modestly increases the overall computational cost.⁴⁹ Although the issue of how to correctly model the compensating counter-charge remains unresolved, these proceedings bear the promise of revoking the need for *post hoc* correction of canonical simulations to approximate grand canonical conditions in future studies.

2.3. Computational Methods. **2.3.1. Model System.** The Volmer–Tafel hydrogen evolution mechanism was studied on a (6×6) Pt(111) surface slab composed of five atomic layers illustrated in Figure 1a. The model electrode containing 180 Pt atoms was solvated using 160 explicit water molecules, resulting in a solvent film thickness of roughly 20 Å. A vacuum layer of 20 Å was further added above the solvent phase in order to decouple periodic images in the direction of the surface normal. The platinum lattice constant was computationally optimized in a previous study,¹⁹ yielding a value of 3.98 Å which corroborates experimental estimates (3.92 Å) and accurate full-potential (linearized) augmented plane wave and local orbitals (FP-(L)APW+lo) results (3.985 Å).⁵⁰ In simulating the Volmer reaction, one excess hydrogen atom was added to the interfacial water layer, resulting in a proton concentration of roughly 0.3 mol l⁻¹ upon spontaneous donation of the lone electron to the metallic surface. Underpotential deposited (UPD) coverages of hydrogen of 2/3 and 1 ML (24 and 36 hydrogen atoms, respectively) were employed to model the most relevant surface saturations at the thermodynamic equilibrium potential of HER. The values above refer to the coverages after the Volmer reaction and prior to the Tafel reaction. While the Tafel step formally requires two hydrogen adatoms, we note that the free energy profile of the Volmer reaction was explicitly simulated only for a single adsorption step. Consequently, the Tafel reaction was assumed to proceed by the recombination of this adatom with a thermoneutrally preadsorbed hydrogen species.

We note that the appropriate equilibrium UPD coverage on Pt(111) at HER operating conditions has been the subject of debate in the literature based on different experimental^{27,51–53} and computational^{11,19,20,26,54,55} conclusions. Per the tradi-

tional view, the UPD hydrogen refers to adatoms that bind strongly to the electrode surface at positive potentials, thereby serving as a spectator species not participating in the HER. Conversely, as the potential is shifted cathodically, further hydrogen atoms adsorb which are thought to bind more weakly, possibly into sites distinct from those preferred by the UPD hydrogen, and it is these “overpotential” deposited (OPD) hydrogens that participate in the HER. While some theoretical¹³ and experimental⁵² efforts have proposed that the site responsible for binding the active OPD intermediates corresponds to platinum top-sites as opposed to deep fcc-sites occupied by the UPD hydrogen, recent dynamic simulations reveal that the discernment of two localized states may not be meaningful. Indeed, the distribution of preferential site occupations has been elucidated in our previous work,¹⁹ suggesting facile adlayer dynamics that gradually decrease with increasing coverage. Hydrogen adatoms are concomitantly observed to increasingly favor top-sites, with exclusive top-binding observed at full surface saturation. The hydrogen coverage on Pt(111) at the thermodynamic equilibrium potential of HER is thus highly affected by collective interatomic surface repulsions and entropic effects and less by the envisioned existence of distinct (in)active sites. For consistency, we have nevertheless considered hydrogen adsorption and evolution from platinum top-sites, but we emphasize that no constraints or control was exerted on the spectating adsorbates, which consequently diffuse and switch sites when energetically feasible.

2.3.2. Electronic Structure Calculations. All DFT calculations were performed within the hybrid Gaussian and plane waves (GPW) framework⁵⁶ as implemented in the CP2K/Quickstep electronic structure and molecular dynamics software package.⁵⁷ The validity of the efficient GPW method, especially suitable for running heavy DFT-MD simulations, has been carefully benchmarked against *k*-point plane wave calculations by Santarossa et al.⁵⁸ Ideally, to obtain fully converged results for surface platinum $8 \times 8 \times 8$ supercells should be employed. This is, however, infeasible for dynamic calculations, and even more so in the present case where a total of roughly one million time steps are simulated. Thus, the system size employed herein has been chosen for a reasonable balance between speed and accuracy. Notably, while the present approach is likely to slightly underestimate surface layer relaxation and surface energies, the total density of states, work function, as well as the d-band center and filling are adequately reproduced as compared to plane wave calculations and experiments.⁵⁸

The expansion of the electron density in the auxiliary plane wave basis was truncated using an energy cutoff of 500 Ry. The 5s, 5p, 5d and 6s electrons of platinum, 2s and 2p electrons of oxygen and the 1s electron of hydrogen were considered valence states and expanded in molecularly optimized double- ζ plus polarization quality Gaussian basis sets (MOLOPT-SR-DZVP).⁵⁹ The remaining ionic cores were represented by norm-conserving Goedecker–Teter–Hutter (GTH) pseudopotentials.^{60–62} The revised⁶³ formulation of the Perdew–Burke–Ernzerhof⁶⁴ density functional approximation (RPBE) was applied in conjunction with DFT-D3 dispersion corrections by Grimme et al.⁶⁵ as deemed suitable for metal–water interface and adsorption simulations due to reduced overbinding and overstructuring effects.^{18,19,21} The dispersion interaction between platinum–platinum pairs was, however, excluded in view of its known incorrect screening

behavior within the metal.^{21,66,67} Traditional matrix diagonalization was used to solve the Kohn–Sham equations and the electronic structure convergence was further accelerated by applying Fermi–Dirac smearing using an electronic temperature of 1000 K as well as the efficient ELPA library of diagonalization routines.⁶⁸ Convergence criteria of $2.7 \cdot 10^{-5}$ eV and $2.3 \cdot 10^{-2}$ eV Å⁻¹ were used for energies and forces, respectively.

2.3.3. Reaction Path Simulations. Constrained Born–Oppenheimer molecular dynamics simulations were conducted within the canonical (NVT) ensemble at a target temperature of 300 K maintained by a CSVR thermostat.⁶⁹ Each constrained MD simulation was run for a minimum of 10 ps, of which the first picosecond was considered equilibration and excluded from the analyses. The interfacial models used herein were taken from a previous extensive unconstrained DFT–MD study of the hydrogen covered Pt(111)–water interface,¹⁹ thus assuring well equilibrated initial solvent structures. A time step of 0.5 fs was employed and the two lowest Pt-layers were frozen to mimic bulk behavior. The SHAKE algorithm⁷⁰ was applied for integrating the Newtonian equations of motion of the systems subject to the defined constraints. The constrained simulations were monitored closely to ensure the satisfactory performance (flexibility and sufficient control) of the defined reaction coordinates. While none were encountered, revised coordinates would have been subject to testing in the occurrence of major issues. A further discussion on observed minor adverse events is given in the [Supporting Information](#).

We note that in acidic solvents the excess protons shuttle between water molecules, deeming the discernment of one hydrogen atom infeasible. In order to eliminate the resulting possibility of undesired water reduction, the individual DFT–cMD trajectories sampling the Volmer step were constructed sequentially starting from the adsorbed state. Each constraint was simulated for a few hundred femtoseconds before using the last frame as a starting point for the following constrained trajectory. This way proton transfer was ensured to occur between the surface and the labeled solvated proton complex, thus revoking the need to apply additional biasing restraints to control untimely Grothhuss diffusion.¹⁴

To establish a static baseline for the dynamic simulations, the Volmer–Tafel MEPs were modeled using the climbing-image nudged elastic band method.^{15,16} Both reactions were partitioned into 10 replicas and each image was optimized until the maximum force reached a value less than 0.05 eV Å⁻¹. Frozen solvent configurations were employed based on snapshots taken from the dynamic simulations. The initial and final states of the elementary reactions were prepared following two distinct approaches; 1) fully optimizing the *initial* state, constraining the solvent structure at this configuration and optimizing the final state only with respect to the reacting atoms (Pt adsorption site(s) and H₂O₃⁺ or 2H*), or 2) fully optimizing the *final* state, constraining the solvent structure at this configuration and optimizing the initial state only with respect to the reacting atoms. This 2-fold approach was taken to mitigate the ambiguity in defining the initial and final states for an inherently dynamic system and consequently to assess the effect of the solvent structure on the MEPs. Each obtained transition state was finally verified by normal mode calculations to exhibit only one imaginary vibrational frequency along the reaction coordinate.

2.3.4. Electrode Potential and Population Analysis. The definition of Trasatti⁷¹ was applied to evaluate the absolute

electrode potential in each of the performed simulations as required by [Equation 7](#). Given our interfacial model of a solvated Pt(111) electrode with periodic copies in the direction of the surface normal separated by vacuum, the absolute electrode potential was calculated from

$$U = \frac{-\mu + e\psi^S}{e} \quad (8)$$

where μ denotes the electrode Fermi level, ψ^S the laterally averaged electrostatic potential in the vacuum region outside the solvent layer, i.e. the Volta potential, and e the elementary charge. The values of the Fermi level and the Volta potential were sampled every 100 fs and a surface dipole correction⁷² was applied in order to account for the artificial electric fields formed across the studied asymmetric interfaces. The obtained absolute electrode potentials were averaged and further converted to the experimentally relevant standard hydrogen electrode (SHE) scale by subtracting 4.44 V as recommended by Trasatti and IUPAC⁷¹ and closely corroborated by Fawcett⁷³ as well as Reiss and Heller.⁷⁴ It is appropriate to note that this value for the absolute potential of the standard hydrogen electrode has been nevertheless somewhat disputed considering the large dispersion of values (3.90–4.85 eV) reported in the literature.^{75–81} Consequently, it has been suggested that methodology-dependent values should be adopted in computational studies for improved consistency.⁸² Our use of the aforementioned reference is however motivated considering the recent work of Sakong and Groß¹⁸ who report a convincing estimate that exactly aligns with the recommended value of 4.44 V. Most importantly, their study applies an identical explicitly dynamic computational setup as herein, including the same exchange–correlation functional, dispersion corrections and model system size, making the reported value essentially the appropriate methodologically consistent absolute potential reference for our study.

The surface charge of the Pt(111) electrode including adsorbates was last calculated using the density derived electrostatic and chemical (DDEC) charge partitioning scheme.^{83,84} To this end, the electron densities of the simulated systems were sampled together with the electrostatic potential every 100 fs and the thereof calculated surface charges averaged. By construction, the DDEC population analysis yields chemically meaningful net atomic charges that reproduce the electrostatic potential of both periodic and aperiodic systems. Most importantly, the obtained charges are basis set independent and have been found to compare favorably with the widely used partitioning theory of Bader.⁸⁵

3. RESULTS AND DISCUSSION

In the following Section we present the reaction pathway and energetics of the Volmer–Tafel mechanism as obtained through the DFT–cMD simulations and the thermodynamic integration procedure. The electrode potential dependence of the Volmer step is approximated in [Section 3.2](#) and used to evaluate experimentally meaningful constant potential estimates for the reaction barrier at the studied hydrogen coverages. The uncertainty associated with the constant potential correction is quantified in [Section 3.2.1](#), followed by a critical discussion on the significance of the obtained results in the light of previous computational and experimental studies in [Section 3.3](#). The convergence of the DFT–cMD simulations as well as the results pertaining to the NEB

minimum energy path optimizations are detailed in the Supporting Information.

3.1. Constrained Molecular Dynamics Simulations.

The averaged forces of constraint are plotted in Figures 2a and

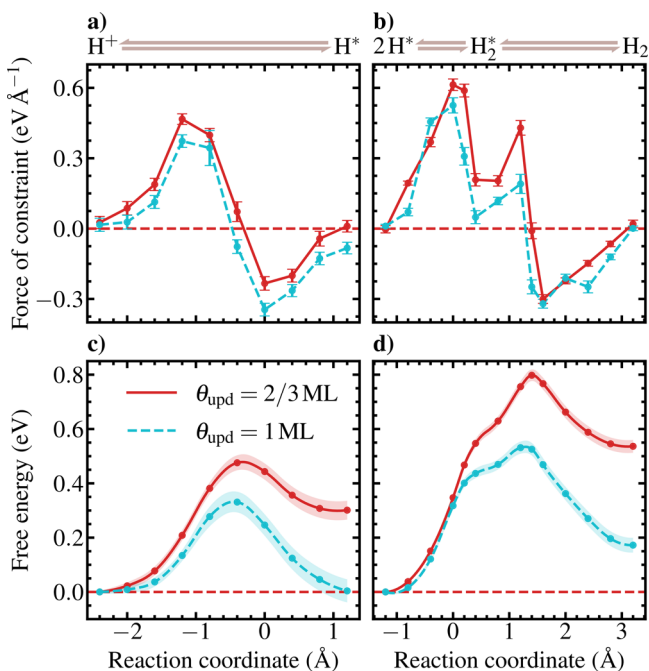


Figure 2. Mean force of constraint and free energy profiles as obtained from the DFT-cMD simulations of the (a,c) Volmer and (b,d) Tafel reactions. The error bars in a and b correspond to margins of error calculated using a block averaging procedure to account for the correlation within the data. Similarly, the shaded areas in panels c and d denote the margins of error obtained by propagating the uncertainty in the mean forces of constraint. In all cases, a confidence level of 95% is implied. The initial and final states as well as the location of the intermediate Kubas complex along the Tafel reaction coordinate are annotated above the upper panels. Note that the electrode potential and surface charge are different at each point along the Volmer coordinate due to the canonical nature of the simulations. The corresponding averaged values are shown in Figure 4.

2b for both of the examined elementary steps and coverages. On the reactant (H^+/H^*) side of the reaction coordinates the forces are positive as the systems are kept from relaxing back to

the reactant minima. Conversely, on the product side (H^*/H_2) relaxation to the final state equilibrium configurations is suppressed and the observed constraint forces are oppositely directed.

While the transition states in Figures 2a and 2b are characterized by the zero force inflection points, an intriguing local minimum is observed prior to the transition state in the Tafel constraint force profile. Visualizing the trajectories reveals that either of the recombining hydrogen atoms, which initially preferentially occupy adjacent Pt top-sites, diffuses to occupy the same top-site as the other hydrogen intermediate as the reaction is driven forward. The doubly occupied Pt atom corresponds to a Kubas PtH_2 -type (H_2^*) complex characterized by nonclassical 2-electron, 3-center bonding between the two σ -electrons of the H_2 molecule and the metal d-orbital.⁸⁶ An identical side-on bonding $\eta^2\text{-H}_2$ complex has recently been observed by Van den Bossche et al. as a metastable intermediate state of the Tafel reaction on the missing-row reconstructed $\text{Pt}(110)\text{-}(1 \times 2)$ surface based on NEB calculations.¹² Our observation represents, however, the first time a Kubas complex has been reported as a transient state of the Tafel reaction on the close-packed $\text{Pt}(111)$ electrode based on a fully dynamic DFT approach. We emphasize that by no means were the hydrogen atoms enforced to occupy the same Pt-site, but only to decrease their mutual separation while increasing the perpendicular distance to the Pt surface in accordance with Equation 6. At a full monolayer hydrogen coverage, the Kubas complex is characterized as a stretched H_2 molecule with an average bond length of roughly 1.1 Å and a perpendicular distance of 1.5 Å to the Pt surface. Decreasing the coverage to 2/3 ML increases the average distances slightly by 0.05 Å. These distances fall in between what has been denoted as “true” and elongated dihydrogen complexes based on nuclear magnetic resonance and crystallographic measurements, suggesting that there is appreciable back-donation from the filled metal d-states to the antibonding σ^* -orbital of H_2 .⁸⁶ This is expected considering the high catalytic activity of Pt toward H_2 dissociation. In addition to the geometry of the observed Kubas intermediate, Figure 3 illustrates schematically the structural details of the other key states along the investigated Volmer–Tafel HER pathway.

Integrating the constraint force profiles of Figures 2a and 2b yields the Helmholtz free energy surfaces plotted in Figures 2c

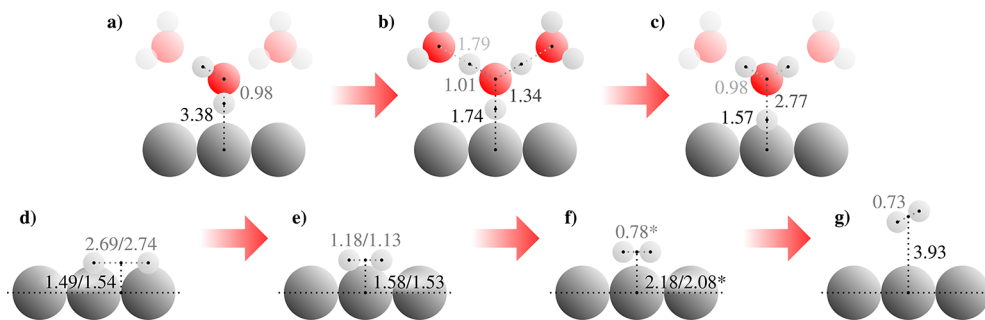


Figure 3. Schematic illustration of the geometries of the (a) initial, (b) transition, and (c) final states of the Volmer reaction as well as the (d) initial, (e) Kubas intermediate, (f) transition, and (g) final states of the Tafel reaction. The first and second values of average interatomic distances (Å) reported for certain geometries correspond to the 2/3 and 1 ML covered surfaces, respectively. Only one value is given if these differ by at most 0.01 Å. Note that the average geometries of the water molecules in a–c are highly symmetric, and therefore, only one set of values is reported for each equivalent bond. The dotted interatomic distances and annotated values are color coded accordingly. In (f), the asterisk denotes that the interatomic distances for the 1 ML covered system were interpolated based on the successive points between which the transition state is located.

and 2d. The associated reaction free energies ($\Delta_r A$) and barriers ($\Delta^\ddagger A$) are summarized in Table 1 together with

Table 1. Canonical Reaction Free Energies ($\Delta_r A$) and Barriers ($\Delta^\ddagger A$) for the Volmer and Tafel Reactions as Well as the Estimated Formation Energy of the Kubas Complex at the Investigated Hydrogen Coverages^a

Reaction	Coverage (ML)	$\Delta^\ddagger A$ (eV)	$\Delta_r A$ (eV)
Volmer	2/3	0.48 ± 0.03	0.30 ± 0.03
	1	0.33 ± 0.04	0.00 ± 0.04
Tafel	2/3	0.80 ± 0.02	0.54 ± 0.02
	1	0.53 ± 0.02	0.17 ± 0.03
Kubas ^b	2/3	0.55 ± 0.02	
	1	0.44 ± 0.02	

^aMargins of error are as specified in Figure 2. The sampling error is in all cases less than the resolution limit of roughly 0.1 eV commonly attributed to standard DFT methods. ^bFormation energy of the Kubas complex prior to H₂ desorption.

margins of error propagated from the uncertainty in the mean forces considering a 95% confidence level. Surprisingly, both the reaction barrier and energy of the Volmer reaction are observed to decrease as the coverage is incremented, contradicting the general view of increasing interatomic repulsions as a function of hydrogen coverage with the opposite effect on the energies.^{19,27,87} As will be demonstrated later in Section 3.2, this apparent anomaly arises due to the as of yet missing constant electrode potential corrections. The free energy profile of the purely chemical Tafel reaction can nevertheless be discussed based on the present canonical results. We note, however, that although the Tafel reaction itself does not directly depend on the electrode potential, an indirect dependence exists due to the potential dependence of the hydrogen coverage through the electrochemical Volmer reaction. Indeed, the increasing lateral repulsions decrease the reaction free energies and barriers of the Tafel reaction by more than 0.3 eV as the coverage is incremented, which is realized in practice by negatively shifting the electrode potential. We note that the increased repulsion contains an entropic component arising from the decreased mobility of hydrogen adsorbates on the fully covered electrode as discussed previously.^{19,88} The stationary adlayer destabilizes the reactant state, thus decreasing the entropic barrier of the forward reaction compared to the unsaturated electrode with more pronounced surface dynamics.

The local force minima associated with the formation of the Kubas intermediates in Figure 2b translate to shoulders in the corresponding free energy profiles upon thermodynamic integration. As the forces do not cross the zero level, no clear free energy minima are observed, highlighting the metastable nature of the intermediate state. Our observations concerning the dynamic Tafel reaction can be compared with the results of Yang et al.⁸⁹ who report aqueous phase activation free energies of 0.53 ± 0.03 and 0.4 eV based on experimental measurements and blue moon ensemble DFT-cMD simulations, respectively. The reverse, dissociative adsorption reaction is on the other hand suggested by both methods to be practically barrierless. A high hydrogen surface coverage is implied and as the catalyst in the experiments the authors employ supported Pt nanoparticles while a close-packed Pt(111) slab is used in the simulations. Considering the 1 ML saturated electrode studied herein, a reassuring agreement

is found with the forward barriers despite the dissimilar microstructure of the experimental system. The high activity of the Pt nanoparticles is, however, reflected in the negligible barrier of the reverse reaction, while for the theoretical result the decreased barrier is likely a consequence of differences in the applied reaction coordinate and/or exchange-correlation functional. An elevated temperature of 343 K and hydrogen partial pressure of $9 \cdot 10^3$ bar are furthermore considered, with the latter realized through the explicit inclusion of excess molecular hydrogen in the solvent phase.

3.2. Electrode Potential Dependence of the Volmer Reaction. The average surface charge and electrode potential at each constraint value along the Volmer reaction coordinate are presented in Figure 4. As the reaction is driven in the

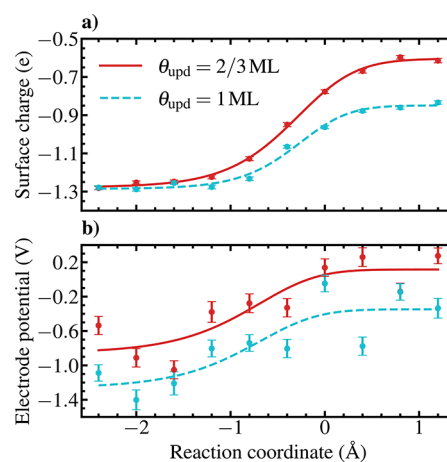


Figure 4. Variation of the electrode (a) surface charge (DDEC) and (b) potential vs SHE along the Volmer reaction coordinate. The plotted values are averages of data sampled every 100 fs from the performed DFT-cMD simulations. Logistic functions according to eq 9 have been fitted to the data, and the error bars denote margins of error at a 95% confidence level. Although the best fits to the electrode potential appear to fall within the error bars for only 3 of the 10 data points, we emphasize that the uncertainties do not correspond to standard deviations, which are substantially larger on the order of 0.5 V.

cathodic direction, charge is transferred from the electrode to the adsorbing proton, resulting in a progressively more positive net charge on the electrode as elaborated in Section 2.2. Without open boundaries, *i.e.* a grand canonical ensemble, no compensating charge is allowed to flow to the electrode, and consequently the increasing positive charge is reflected also as an increasing electrode potential. The functional form of the varying surface charge in Figure 4a is sigmoidal and we have therefore fitted the generalized logistic function of Equation 9 to the data,

$$\hat{q}(\xi) = a + \frac{b - a}{(1 + e^{-r\xi})^\nu} \quad (9)$$

where a and b are the lower and upper asymptotes, respectively, r the growth rate and ν a parameter affecting the position of the maximum growth. An equivalent function $\hat{U}(\xi)$ with $r = 2 \text{ \AA}^{-1}$ and $\nu = 4$ was also applied for the electrode potential motivated by the good fit of the logistic model to the surface charge data and the NEB electrode potentials presented in the Supporting Information (Figure S3). Interestingly, the desorbed states exhibit identical surface

charges while the surface charges of the adsorbed states differ by roughly 0.22 e. This indicates that either the charge transfer process is less complete on the 1 ML covered surface with only 0.45 e transferred to the adsorbing proton, or that the average interfacial structures of the adsorbed states differ such that an excess charge localization on the 1 ML covered Pt(111) electrode is favored, or a combination thereof. The apparent fractional charge transfer between a metal electrode and a protonated solvent has been proposed by Chen et al.⁹⁰ to arise from a distance dependent hybridization of the metal d-band with the hydrated proton. By evaluating the degree of charge transfer using both semilocal and hybrid exchange-correlation functionals, as well as high-level embedded correlated wave function methods, the authors show that the fractional charge transfer is not due to spurious electron delocalization owing to DFT self-interaction error, but a physical effect that decreases in magnitude as the proton is transferred farther from the surface. As also discussed by Lindgren et al.,¹³ no fractional charges are expected for the limiting case of a proton solvated in bulk water, i.e. the “true” initial state of the Volmer reaction. In our case the electron spillover should, however, be more suppressed on the fully covered electrode due to screening by the hydrogen adlayer as well as the increased surface–solvent separation.¹⁹

Nonetheless, the delicate charge distribution at the interface is ultimately governed by the minimum energy principle, which here implies that the enforced hydrogen coverage must be stabilized by a suitably balanced water dipole distribution (orientational effect) and interfacial charge transfer (electron redistribution effect) which together determine the equilibrium electrode potential.²² Indeed, in electrochemical systems the surface coverage, charge and electrode potential are interrelated, and it is strictly speaking not possible to alter one without affect the other variables. Considering the final (adsorbed) states, our results show that there is a net transfer of 0.6–0.8 e from the (neutral) water contact layer to the electrode depending on the coverage and the interfacial dipole. The resulting equilibrium electrode potentials plotted in Figure 4b reveal that the stabilization of the 1 ML covered Pt(111) electrode requires a roughly 0.4 V more negative potential compared to the unsaturated surface. However, whereas the electrode surface charges are found to be rather stable during the course of each simulation, the electrode potential fluctuates substantially due to the considerable thermal motion of the interfacial solvent as repeatedly reported in the literature.^{14,18,54} As a consequence of the variable surface dipole, the average electrode potentials are challenging to converge and thus more scattered with respect to the fitted logistic functions in which the parameters r and ν were fixed (*vide supra*) to avoid overfitting. Although the uncertainty in the electrode potential fits and its implications on the potential dependence of the Volmer reaction will be analyzed in further detail in Section 3.2.1, the overall trend agrees with the surface charges, i.e. the electrode potential increases as the Volmer reaction progresses in the cathodic direction and charge is transferred from the metal to the adsorbing proton.

Performing the Chan–Nørskov charge extrapolation as outlined in Sections 2.2 and 2.3.4 using the above fitted surface charge and electrode potential models yields the potential dependence of the free energy surfaces presented in Figures 5a and 5b. We note that a more straightforward and perhaps conventional approach would be to apply the charge extrapolation of Equation 7 directly in a point-by-point fashion

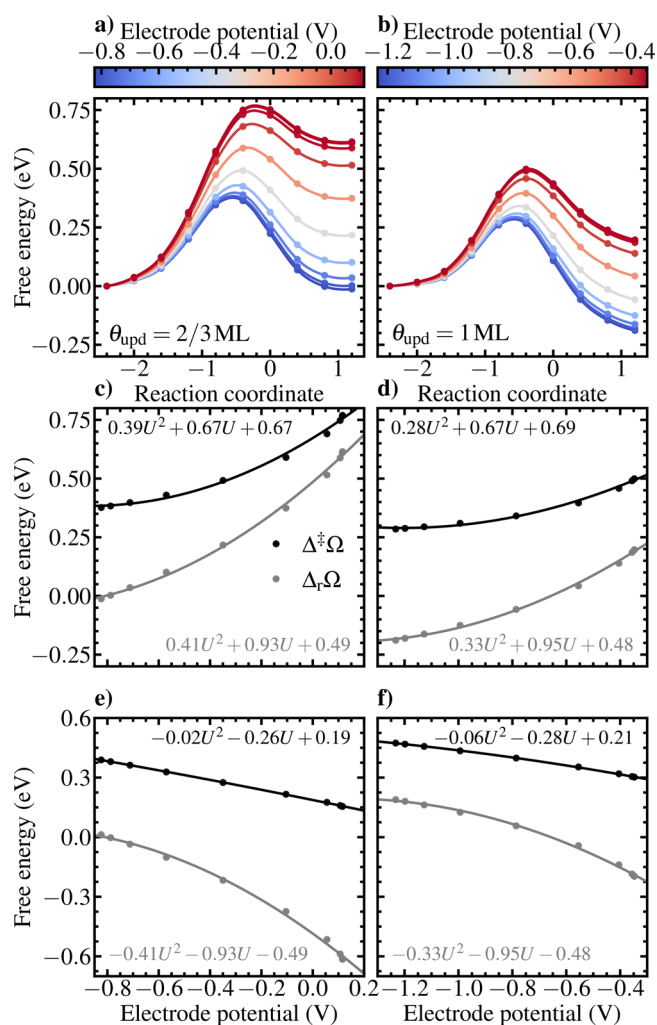


Figure 5. Electrode potential dependence of the Volmer free energy surfaces at (a) 2/3 ML and (b) 1 ML hydrogen coverages. The parabolic potential dependence of the reaction free energies and barriers is expressed separately for the (c,d) forward (cathodic) and (e,f) reverse (anodic) directions at (c,e) 2/3 ML and (d,f) 1 ML hydrogen coverages together with fits according to eq 10. Electrode potentials are reported vs SHE. Note the different potential scales on the color bars.

instead of using the fitted model functions. While certainly possible, we argue that such a direct application would yield qualitatively inconsistent electrode potential dependencies. Indeed, inspecting the averaged electrode potentials in Figure 4b reveals that at several instances the potential *decreases* in spite of the surface charge *increasing*. This is due to the slow convergence of the electrode potential requiring substantially longer DFT-MD simulations to exhaustively sample all relevant solvent orientations at a given electrode potential. As this is beyond current available computational resources, we treat the electrode potential data as a whole and consider that the data on average reflects the expected behavior where driving the reaction forward results in an increased electrode potential as negative charge is transferred from the surface to the adsorbing proton. Reassuringly, the best fits to the data in Figure 5b confirm this average behavior as discussed above. We emphasize also that the depicted error bars correspond to standard errors of the mean at a confidence level of 95%, and

not standard deviations reflecting the true variability of the sampled electrode potentials on the order of 0.5 V.

Expectedly, the barriers and reaction free energies of the cathodic Volmer reaction are found to decrease as the electrode is polarized negatively, while the opposite trend applies for the reverse, anodic direction. Explicitly visualizing the potential dependence of the reaction barriers and energies in Figures 5c and 5d reveals a marked parabolic shape, originating from the employed capacitive model of the electrostatic contribution. We note that this behavior of the activation free energy is qualitatively consistent with the Marcus–Hush theory of charge transfer kinetics.^{91,92} To quantify this quadratic dependence, we have fitted second degree polynomials to the data including the reverse reactions illustrated in Figures 5e and 5f,

$$\hat{\Omega}_i(U) = \alpha_i U^2 + \beta_i U + \gamma_i \quad (10)$$

where the subscript i separates the different reaction directions and the constant term γ_i can be identified as the barrier and reaction energy values at 0 V vs SHE. For the forward Volmer reaction the barriers are approximately 0.67 and 0.69 eV on the 2/3 and 1 ML saturated electrodes, respectively, whereas the corresponding reaction energies are 0.49 and 0.48 eV. These results indicate a relatively mild coverage dependence at the thermodynamic HER equilibrium potential. Reassuringly, the applied charge extrapolation explains and corrects the anomalous observation that the apparent barriers and reaction free energies of the Volmer step would according to Figure 2 decrease with an increasing coverage despite previously recognized growing lateral repulsions. The root cause of this evident inconsistency is thus in the markedly more negative electrode potential required to stabilize the surface saturated by hydrogen as illustrated in Figure 4b. Consequently, the striking importance of electrode potential considerations in the simulation of electrochemical reactions is again highlighted.

As a side remark, we underscore that both obtained reaction free energies of the Volmer step are positive at 0 V vs SHE, indicating that the presumed active hydrogen intermediates are bound endergonically on the Pt(111) surface. This corroborates the results of Lindgren et al.¹³ as well as Exner^{93,94} who propose that the active hydrogen participating in the HER do not correspond to thermoneutrally ($\Delta_r G = 0$ eV) bound species as originally suggested.⁹⁵ While other studies⁹⁶ have implied that the apex of the activity volcano could also be located at negative values, indicating exergonic adsorption to be important for facile hydrogen evolution, the dynamic computational methodology employed in the present work supports nevertheless the recent conclusions of HER active hydrogen intermediates being weakly bound.

It is also possible to evaluate the charge transfer coefficient by differentiating the free energy barrier with respect to the electrode potential.^{12,26} Subsequently, the cathodic transfer coefficients are found to vary linearly between 0.7 and 0.5 as the potential is scanned from 0 V to -0.2 V vs SHE. This entails that the transition state of the Volmer reaction becomes increasingly more final state-like around the equilibrium potential. Similarly, both anodic charge transfer coefficients are found to remain close to 0.3 within the same potential window, conversely indicative of an “early” transition state. Although the linear potential dependence is theoretically justified considering the parabolic free energy barrier curves, the obtained values align well with the frequently made

assumption that the transfer coefficients attain relatively constant values around 0.5. We note that the cathodic and anodic transfer coefficients do not, however, add up to 1 for the more negative potentials due to fractional charge transfer induced by the hybridization of the metal d-band with the protonated interfacial solvent as discussed before.⁹⁰

3.2.1. Error Analysis. The dispersion of the averaged electrode potentials in Figure 4b indicates that there is considerable uncertainty associated with the potential dependence caused by the slow convergence of the quantity. Notably, while the error bars denoting margins of error at a 95% confidence level may appear modest, we reiterate that the standard deviations of the potential fluctuations are on the order of 0.5 V for each sampled trajectory. Consequently, it is informative to perform a sensitivity analysis of the logistic fits and the consequent impact on the charge extrapolated free energy barriers of the Volmer reaction at 0 V vs SHE. To this end, we perform the following two step statistical analysis. First, a bootstrap resampling procedure is conducted to evaluate the sensitivity of the model function with respect to the averaged electrode potentials. Specifically, 10 random values along the reaction coordinate are sampled *with replacement* such that each corresponding electrode potential can be obtained zero or multiple times, effectively yielding a new resampled data set of average electrode potentials to which the logistic function of the form 9 is fitted. This resampling process is repeated 10^4 times in order to obtain probability distributions of the fitting parameters a and b , i.e. the lower and upper asymptote values. The results are visualized in Figure 6.

Following the bootstrapping, a Monte Carlo method is applied to propagate the uncertainties associated with the electrode potential fits through the charge extrapolation procedure for the respective coverages. To this end, the obtained lower and upper asymptote distributions are sampled 10^6 times to generate an ensemble of trial electrode potential models using which the charge extrapolation is repeatedly performed. This yields a distribution of potential corrected free energy profiles from which the margins of error of the accordingly distributed free energy barriers can be calculated. In addition to considering the charge extrapolation error due to the scattered electrode potentials, a separate Monte Carlo uncertainty propagation is performed in which the sampling error of the forces of constraint affecting the results of the thermodynamic integration is also accounted for. Thus, we are able to decouple the uncertainties arising from the constrained MD simulations and the charge extrapolation scheme and gauge which of the methods constitutes the dominating source of error. The results are summarized in Table 2.

Considering only the uncertainty related to the electrode potential fits, the cathodic Volmer reaction barriers at 0 V vs SHE with margins of error are 0.67 ± 0.11 eV and 0.69 ± 0.16 eV for the 2/3 and 1 ML covered surfaces, respectively, while for the reverse reaction the values 0.19 ± 0.04 eV and 0.21 ± 0.08 eV are acquired. Including the uncertainty in the canonical free energy profiles increases the margins of error by up to 0.04 eV, demonstrating the predominant effect of the electrode potential on the total error estimate. This result is also clearly shown by summarizing the free energy barriers of the simulated elementary reactions including the obtained barriers for the chemical Tafel step in Figure 7. Indeed, the margins of error associated with the constraint force sampling of both the forward and reverse Tafel reactions are on the

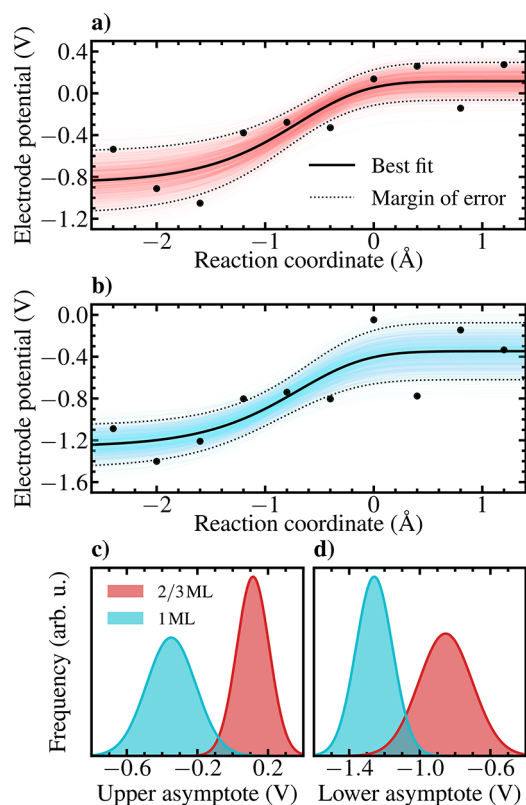


Figure 6. Bootstrap resampling of the averaged electrode potentials of the (a) 2/3 ML and (b) 1 ML hydrogen covered interfaces. The best fit obtained by considering all electrode potentials along the reaction coordinate is indicated in both panels together with the ensemble of fits to each bootstrap resample (faint colored lines) and the resulting margins of error at a 95% confidence level. The resulting distributions of the (c) upper and (d) lower asymptote fitting parameters are illustrated as probability density functions smoothed with a Gaussian kernel.

Table 2. Free Energy Barriers of the Cathodic and Anodic Volmer Reactions at the Investigated Hydrogen Coverages at 0 V vs. SHE^a

Direction	Coverage (ML)	$\Delta^{\ddagger}\Omega^{\circ}$ (eV)	CE error	CE + TI error
Cathodic	2/3	0.67	± 0.11	± 0.11
	1	0.69	± 0.16	± 0.20
Anodic	2/3	0.19	± 0.04	± 0.05
	1	0.21	± 0.08	± 0.12

^aMargins of error are estimated by a Monte Carlo approach from the uncertainties associated with the charge extrapolation (CE) and thermodynamic integration (TI) methods. A confidence level of 95% is implied.

order of 0.01–0.02 eV, i.e. nearly one magnitude less than for the Volmer reaction including the charge extrapolation error.

3.3. Comparison with Barriers from NEB Calculations and Experimental Activation Energies. Static MEP calculations suffer from ambiguous solvent structure choices and lack of entropic contributions due to quenched interfacial fluctuations. We admit, however, that the dynamic approach based on constrained MD simulations also suffers from its own limitations related to overestimation of long-range solvent reorganization as discussed later in this Section. Thus, the two methods represent very different imperfect means of simulating reaction paths with their own rather opposite shortcomings.

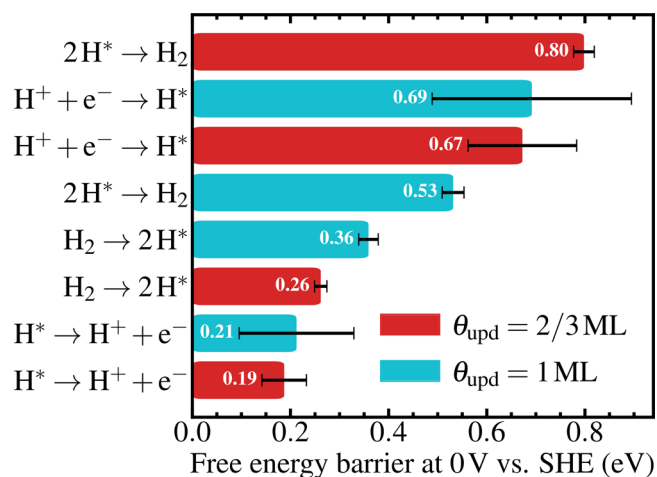


Figure 7. Determined free energy barriers of the cathodic and anodic Volmer–Tafel mechanisms at the studied hydrogen covered Pt(111) electrodes. The margins of error at a 95% confidence level include the uncertainties related to the sampled forces of constraint (thermodynamic integration error) as well as the electrode potentials in case of the electrochemical Volmer step (charge extrapolation error). Note that the plotted values refer to the free energy barriers of the elementary Volmer and Tafel steps and not the rate-determining effective activation free energies set by the transition states highest in energy.

The former issue of the static procedure is illustrated clearly by the performed reference NEB calculations for the Volmer reaction at the two investigated hydrogen coverages (Figure S2). Depending on whether the solvent structure is optimized according to the initial or final states, differences as large as 0.3 and 0.5 eV are observed for canonical barriers and reaction energies, respectively. This discrepancy remains after the subsequent charge extrapolation to constant electrode potential (Figure S4). As discussed in our previous work,¹⁴ the solvent structure optimized at the geometry of the initial state leads to considerably higher reaction barriers and energies due to steric hindrance imposed by the frozen solvent of the final state. Conversely, constraining the solvent into the structure of the final state results in an excessively destabilized initial state. These examples illustrate extreme cases that may emerge when static calculations are performed in order to estimate MEPs of reactions occurring at inherently dynamic conditions. Consequently, the “true” MEP can be expected to reside in between the limiting results and a first order approximation is attained by straightforward averaging. For the forward Volmer reaction barrier this would in our case yield the results 0.58 and 0.78 eV at 0 V vs SHE. However, several solvent structures should ideally be considered in the spirit of the transition path ensemble concept⁹⁷ for further improved estimates. Considering the accuracy of barrier heights, the most appropriate solvent structure depends also on whether the reaction has an early or late transition state. Indeed, for a more initial state-like transition state, solvent structures optimized at the initial state configuration are more likely to yield a reliable barrier.

In contrast, the Tafel reaction shows little dependence on the solvent structure as the NEB calculations yield barriers ranging from 0.8 to 0.9 eV irrespective of coverage. While the solvent independence is expected due to the Tafel reaction being a homolytic Langmuir–Hinshelwood type surface reaction, the mild coverage effect is surprising as the saturated

electrode should exhibit more pronounced lateral surface repulsions that destabilize the initial state. This discrepancy with our dynamic simulations is most likely a result of the missing entropic contributions affecting the reactant and product state stabilities through the differing adlayer dynamics¹⁹ as discussed in Section 3.1. Indeed, without entropic considerations the decreasing effect of surface repulsion on the Tafel reaction barrier has been reported to become prominent only for coverages strictly larger than 1 ML.^{11,26}

In general, our static NEB results for the Volmer and Tafel reactions align well with previous computational studies of HER on Pt(111). Employing the size extrapolation scheme and an ice bilayer model of the solvent, Skúlason et al.¹¹ conducted one of the first comprehensive kinetic modeling attempts of the HER, reporting barriers of 0.69 and 0.85 eV for the Volmer and Tafel reactions, respectively, at 0 V vs SHE and a coverage of 1 ML. These results were later reproduced and refined by Van den Bossche et al.¹² using implicit solvation calculations in conjunction with a static Eigen cluster model of the hydrated proton and a modified Poisson–Boltzmann description of the counter-charge distribution. Owing to the solvent independence of the Tafel reaction, barrier heights ranging between 0.81 and 0.87 eV were optimized using both bilayer and cluster water models, closely corroborating both previous as well as herein presented static results. However, the cluster model was observed to decrease the Volmer reaction barrier to 0.48 eV compared to the 0.69 eV barrier obtained using the bilayer model. This difference was attributed to the increased flexibility of the cluster model, allowing the system to better maintain its hydrogen bonding network at the transition state in contrast to the more rigid ice bilayer. The bilayer model was nevertheless argued more accurate due to the explicit treatment of the next-nearest neighbor water interactions.

A related “solvated jellium” approach⁴² in which the counter-charge distribution is homogeneously distributed within the implicit solvent was applied by Lindgren et al.¹³ in order to computationally investigate the HER activity of Pt(111). Using a static ice bilayer model of the water contact layer and the NEB method, significantly lower barriers of 0.27 and 0.40 eV were reported for the Volmer and Tafel steps, respectively, at 0 V vs SHE. The markedly lower barrier heights compared to the works of Skúlason and Van den Bossche et al. have been speculated to stem from differences in the applied exchange-correlation functional (PBE vs RPBE), implicit solvation model and constant potential approximations. We note, in addition, that the starting geometries of the Volmer step in particular are rather biased toward the transition state as the initial platinum–proton distance is only 2.3 Å compared to the roughly 4.0 Å separation employed by Van den Bossche et al., possibly affecting the portion of the barriers related to diffusion within the interfacial solvent and fractional charge transfer. Moreover, the fact that Lindgren et al. studied a coverage of more than 1 ML is likely to also play a key part in decreasing the observed barriers through the repulsion-induced weakening of the adsorption strength.

Importantly, comparing the results obtained by our explicitly solvated, fully dynamic simulations summarized in Figure 7 to the aforementioned reference values reveals both intriguing differences as well as unexpected similarities. At 0 V vs SHE, the 0.69 ± 0.20 eV reaction barrier of the cathodic Volmer step at a 1 ML coverage aligns well with the static NEB results

presented here and elsewhere.^{11,12} Similarly, the Tafel barrier at a 2/3 ML coverage of 0.80 ± 0.02 eV is excellently corroborated by the previous results.²⁶ This agreement is surprising given the missing entropic contributions in the static NEB calculations. Considering the Volmer reaction at a 1 ML coverage, the hydrogen adlayer structure is rather stationary, suggesting a substantial entropic barrier for the adsorption step.¹⁹ This increase in the barrier may be suitably compensated by the biased ice bilayer model employed in the NEB calculations, resulting in fortuitous error cancellation. In case of the Tafel reaction, the correspondence between the static and dynamic barriers might on the other hand be a consequence of the similar entropies of the initial and final states due to the pronounced dynamics of the hydrogen adlayer at 2/3 ML coverage.¹⁹ This explains also the difference to the situation at a coverage of 1 ML where the free energy barrier drops to 0.53 ± 0.02 eV due to the stationary adlayer decreasing the entropic barrier associated with the desorption. This effect cannot be observed in the static calculations, which predict a decreased Tafel barrier only at coverages beyond 1 ML.^{11,12,26} We emphasize, however, that this qualitative analysis is tentative and gauging the entropy changes quantitatively would require a thermodynamic assessment of the energetics by running DFT-cMD at multiple simulation temperatures, a task that is beyond the scope of the present study and at the limit of current computational power.

It is confusing that the dynamic Volmer reaction exhibits at the coverage of 2/3 ML a free energy barrier very similar to that observed on the 1 ML covered surface although the mobile adlayer would suggest a decreased entropic barrier and less interatomic repulsions at the final, adsorbed state. Even if neglecting the entropy, the performed NEB calculations indicate also a roughly 0.2 eV smaller barrier height for the unsaturated electrode. We attribute this apparent inconsistency to weaknesses in the employed charge extrapolation scheme. Although the applied constant potential correction indeed shifts the coverage dependence of the canonical barriers toward the expected direction (*vide supra*), the dynamic nature of the water structure allows the solvent to react to the changing surface charge and electrode potential, consequently softening the potential dependence. This damping effect can be observed by comparing the variations in the electrode charge and potential over the course of the dynamic and static reactions plotted in Figures 4 and S3, respectively. However, as discussed above, we believe that a more serious issue is embedded in the electrode potential fluctuations, enabling variations of roughly 0.5 eV in the upper and lower potential asymptotes. This corresponds also to the standard deviation of the potential fluctuations (in units of V) in each of the simulated trajectories. It is nevertheless desirable in the future to extend the charge extrapolation formalism of Chan and Nørskov^{40,41} to account for solvent reorganization, possibly through the inclusion of a term considering the energy change associated with a reorienting interfacial dipole, $\Delta E \sim -\Delta(\mu \cdot E)$.

Notwithstanding, the constrained MD approach has its own clear limitations that need to be acknowledged as mentioned in the beginning of this Section. Indeed, the above damping effect of the electrode potential dependence is a manifestation of the dynamic sampling of the solvent structure where each point along the reaction coordinate is treated independently. A true chemical reaction is in contrast an instantaneous process initiated e.g. by the collision of two species with substantial

kinetic energies. As the local solvent structure is likely unable to respond to such a rapid event, the constrained MD methodology may erroneously reflect unphysical long-range solvent reorganizations. In this sense, thermodynamic integration based on constrained MD trajectories is inferior to NEB calculations. However, we emphasize that the dynamic simulations include entropic effects explicitly, avoiding the need to estimate the finite-temperature contributions *a posteriori* based on e.g. vibrational analyses. The ambiguous choice of frozen solvent configuration is also avoided. Admitting the limitations of both approaches, we note that the only truly rigorous way of simulating chemical rare events would be to sample ensembles of trajectories following the reaction rate theory of Chandler et al.⁹⁷ Unfortunately, techniques aligning with the transition path ensemble concept are currently computationally prohibitively expensive.

Turning to recent experimental results, the apparent activation energy of the HER on Pt(111) reported by He et al.²⁸ is potential dependent and ranges between 0.7 and 0.5 eV as the electrode is cathodically polarized from 0 V to -0.2 V. This value is significantly larger than the seminal value of 0.19 eV reported by Marković et al.,²⁷ further supporting the recently emerging presumption^{12,28} that the therein employed single-crystal electrodes may have been contaminated by a low, but decisive concentration of active defect sites, resulting in a biased interpretation of the hydrogen evolution activity of Pt(111). This is also suggested by a more recent 0.17 ± 0.02 eV estimate of the HER activation energy on carbon supported Pt nanoparticles.⁹⁸

We reiterate that the apparent value of the activation energy obtained from temperature-dependent experiments corresponds to the enthalpic portion of the rate-determining activation free energy.²⁹ To facilitate a tentative comparison of our dynamic results with reported experimental values, we compose the free energy landscape of the Volmer–Tafel HER mechanism on Pt(111) in Figure 8. The rate-determining effective barrier (the activation free energy) obtained herein corresponds to the free energy of the Tafel transition state, $\Omega_{\text{eff}}^{\ddagger} = \Delta^{\ddagger}\Omega_{\text{T}} + \Delta_{\text{r}}\Omega_{\text{V}}$. Indeed, although the free energy barrier of the Volmer elementary step is higher than that of the Tafel step at 1 ML coverage and 0 V vs SHE, the endergonic reaction free energy contributes to a considerable activation free energy of 1.01 eV. At the lower simulated coverage of 2/3 ML the corresponding value is 1.28 eV which appears too large for facile hydrogen evolution. Thus, it is more likely that the relevant coverage at the thermodynamic equilibrium potential of HER is closer to, or even above, 1 ML, which is corroborated by the results of Lindgren et al.¹³ as well as experimental measurements.⁵³ Nonetheless, comparing to the experimental results of He et al. we note that there is clearly a considerable entropic component in the HER activation free energy, as the obtained results are at least 0.3 eV larger than the apparent activation energies including only enthalpic contributions.

Intriguingly, the potential dependence of the Volmer reaction extracted through the charge extrapolation is soft enough that the Tafel step remains rate limiting throughout the illustrated potential range. Nevertheless, Tafel slopes of experimentally measured polarization curves depicting the derivative of the overpotential with respect to the logarithmic current density suggest values around 120 mV dec^{-1} at high overpotentials which does not coincide with a rate determined by the Tafel step (30 mV dec^{-1} , tending to ∞ for large

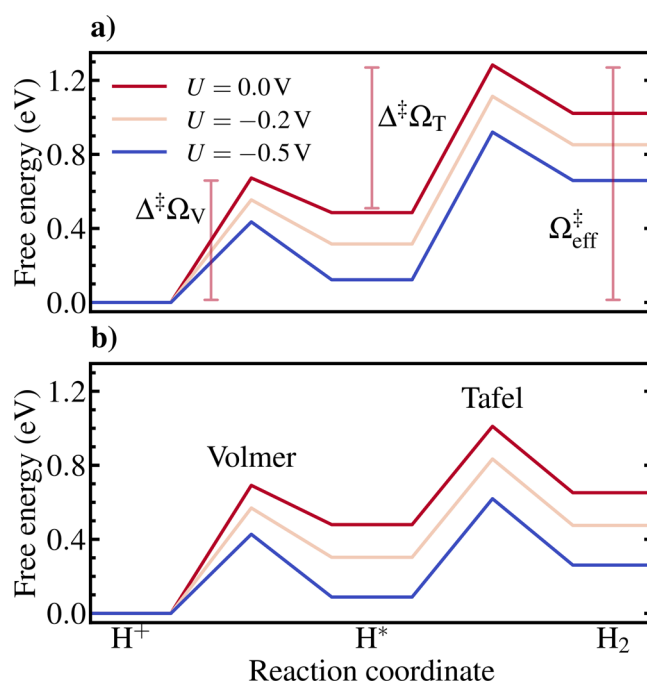


Figure 8. Free energy landscapes of the Volmer–Tafel HER mechanism at (a) 2/3 ML and (b) 1 ML UPD hydrogen coverages. The electrode potential dependence is illustrated at three distinct constant potentials (vs SHE). The free energy barriers of the Volmer and Tafel steps are annotated in a, including the rate-determining effective activation free energy $\Omega_{\text{eff}}^{\ddagger} = \Delta^{\ddagger}\Omega_{\text{T}} + \Delta_{\text{r}}\Omega_{\text{V}}$. Note that the adsorption of only one hydrogen atom is explicitly considered, as the Tafel step is assumed to proceed through the recombination of this hydrogen with a thermoneutrally preadsorbed adatom. The legend in a refers to both panels.

overpotentials).²⁹ Although mass transfer limitations at high overpotentials may complicate the analysis of Tafel slopes and subsequent mechanistic interpretations,⁹⁸ it is possible that the potential dependent decreasing of the reaction free energy of the Volmer step is underestimated as discussed in the context of the limitations of the DFT-cMD approach. Consequently, a shift in the RDS from the Tafel to the Volmer step cannot be concluded from our results. Considering coverages strictly larger than 1 ML could, however, also further decrease the Tafel barrier so that the Volmer reaction would eventually become rate limiting with a theoretical Tafel slope of 120 mV dec^{-1} . Investigating supersaturated surfaces using a dynamic computational methodology as herein constitutes an interesting topic for future research, ideally including also a dynamic treatment of the alternative Heyrovský step and a full-fledged microkinetic model to directly couple the microscopic kinetic parameters with experimental observables.

4. CONCLUSIONS

The simulated hydrogen evolution activity of Pt(111) has been debated widely due to apparent inconsistencies with experimental data²⁷ suggesting up to 4-fold lower apparent activation energies. However, most computational efforts assessing the electrocatalysis of hydrogen on metal electrodes such as Pt(111) consider static interfaces and ice-like solvent models the accuracies of which have not been thoroughly assessed.^{11–13,26} In this work, we demonstrated a successful application of DFT-based constrained MD simulations and thermodynamic integration for reassessing the Volmer–Tafel

hydrogen evolution mechanism on Pt(111) with appropriate consideration of finite-temperature fluctuations, electrode potential dependence and hydrogen coverage effects. Based on our explicitly dynamic approach, the free energy barrier of the Tafel elementary reaction was found to decrease considerably upon increasing the hydrogen coverage to a full monolayer. The stationary hydrogen adlayer on the saturated Pt(111) electrode was interpreted to decrease the reactant state entropy of the Tafel step, thereby lowering the entropic barrier of the desorption in comparison to the situation at the more mobile 2/3 ML covered surface where the initial and final states are highly dynamic and may reflect more similar entropies.

Modeling the electrode potential dependence of the Volmer reaction based on a capacitor analogy^{40,41} enabled the evaluation of kinetic parameters as a function of the applied voltage. The *a posteriori* charge extrapolation reproduced the qualitatively correct potential dependence of both the cathodic and anodic Volmer steps, as well as corrected the inconsistent coverage dependence of the canonical free energy profiles as obtained through the thermodynamic integration procedure. Acknowledging the slow convergence and uncertainty in the averaged electrode potentials and the models fitted to the data, a rigorous two step error analysis based on bootstrap resampling followed by a Monte Carlo-based uncertainty propagation was performed. The error in the extrapolated free energy barriers originating from the electrode potential was found to dominate over the sampling error of the forces of constraint.

Compiled free energy landscapes of the Volmer–Tafel mechanism suggested rather considerable activation free energies of the HER on Pt(111) due to the endergonic adsorption of the active hydrogen intermediate and the still relatively high free energy of the Tafel transition state. While the herein obtained rate limiting activation free energies remain substantially larger than the seminal, yet possibly biased, values presented by Marković et al.,²⁷ a more reasonable correspondence was obtained with the more recent measurements of He et al.²⁸ Considering that the experimentally measured apparent activation energies only contain enthalpic contributions, the entropic component of the simulated activation free energy was deduced to be at least 0.3 eV if considering a hydrogen coverage of 1 ML. An excellent agreement was also found with previous computational studies^{11,12} employing static minimum energy path calculations in cases where entropic effects or errors owing to the employed constant potential model cancel. We emphasize, however, that the performed DFT-cMD simulations are advantageous in avoiding ambiguous solvent structure choices for inherently dynamic systems, thereby decreasing the reliance on fortuitous error cancellation. On the other hand, the limitations of the DFT-cMD approach must be acknowledged as the dynamic sampling was observed to promote overestimated long-range solvent reorganizations resulting in a too soft potential dependence of the electrochemical Volmer step. Consequently, the rate of the HER on Pt(111) was found to be limited by the Tafel step in a wide potential window.

It is evident that the uncertainty in the treatment of the electrode potential presents a persisting hurdle in electrochemical simulations and this challenge is accentuated by the exponential dependence of rate constants on the potential dependent activation free energies. The error associated with the electrochemical barriers was estimated herein to be of

similar magnitude as the resolution limit frequently assigned to semilocal density functional approximations suffering from adverse self-interaction errors. A variation of this magnitude is easily sufficient to result in immense margins of errors for macroscopic current densities. Although the spatial (cell size) and temporal (simulation length) requirements for obtaining tightly converged electrode potentials present a major obstacle together with the lack of a “perfect” functional, workarounds such as charge constrained DFT (cDFT)⁹⁹ and linear-scaling DFT-MD algorithms¹⁰⁰ extending the accessible length scale of routine simulations to more than 10^4 atoms are expected to pave the way for more accurate electrochemical modeling. Until then, the present work represents nevertheless one of the most extensive and realistic simulations of HER on Pt(111) based on an explicit, fully dynamic first-principles approach.

■ ASSOCIATED CONTENT

Supporting Information

The Supporting Information is available free of charge at <https://pubs.acs.org/doi/10.1021/acscatal.1c00538>.

Convergence of constrained MD simulations; results of static reference NEB calculations; variation of surface charge and electrode potential along the Volmer MEPs and results of the subsequent charge extrapolation (PDF)

Machine-readable geometries (.xyz) of all optimized NEB stationary states (ZIP)

■ AUTHOR INFORMATION

Corresponding Author

Kari Laasonen – *Research Group of Computational Chemistry, Department of Chemistry and Materials Science, Aalto University, FI-00076 Aalto, Finland*; orcid.org/0000-0002-4419-7824; Email: kari.laasonen@aalto.fi

Author

Rasmus Kronberg – *Research Group of Computational Chemistry, Department of Chemistry and Materials Science, Aalto University, FI-00076 Aalto, Finland*; orcid.org/0000-0002-6257-5956

Complete contact information is available at: <https://pubs.acs.org/doi/10.1021/acscatal.1c00538>

Notes

The authors declare no competing financial interest.

■ ACKNOWLEDGMENTS

R.K. acknowledges the School of Chemical Engineering of Aalto University for funding in the form of a doctoral scholarship. The authors wish to thank CSC – IT Center for Science, Finland, for the generous computational resources provided through the Mahti supercomputer pilot project.

■ REFERENCES

- (1) Seh, Z. W.; Kibsgaard, J.; Dickens, C. F.; Chorkendorff, I. B.; Nørskov, J. K.; Jaramillo, T. F. Combining theory and experiment in electrocatalysis: Insights into materials design. *Science* **2017**, *355*, eaad4998.
- (2) Magnussen, O. M.; Groß, A. Toward an atomic-scale understanding of electrochemical interface structure and dynamics. *J. Am. Chem. Soc.* **2019**, *141*, 4777–4790.
- (3) Sakaushi, K.; Kumeda, T.; Hammes-Schiffer, S.; Melander, M. M.; Sugino, O. Advances and challenges for experiment and theory for

multi-electron multi-proton transfer at electrified solid-liquid interfaces. *Phys. Chem. Chem. Phys.* **2020**, *22*, 19401–19442.

(4) Calle-Vallejo, F.; Loffreda, D.; Koper, M. T.; Sautet, P. Introducing structural sensitivity into adsorption-energy scaling relations by means of coordination numbers. *Nat. Chem.* **2015**, *7*, 403.

(5) Greeley, J.; Jaramillo, T. F.; Bonde, J.; Chorkendorff, I.; Nørskov, J. K. Computational high-throughput screening of electrocatalytic materials for hydrogen evolution. *Nat. Mater.* **2006**, *5*, 909–913.

(6) Xin, H.; Vojvodic, A.; Voss, J.; Nørskov, J. K.; Abild-Pedersen, F. Effects of d-band shape on the surface reactivity of transition-metal alloys. *Phys. Rev. B: Condens. Matter Mater. Phys.* **2014**, *89*, 115114.

(7) Jinnouchi, R.; Asahi, R. Predicting catalytic activity of nanoparticles by a DFT-aided machine-learning algorithm. *J. Phys. Chem. Lett.* **2017**, *8*, 4279–4283.

(8) Wexler, R. B.; Martinez, J. M. P.; Rappe, A. M. Chemical pressure-driven enhancement of the hydrogen evolving activity of Ni₂P from nonmetal surface doping interpreted via machine learning. *J. Am. Chem. Soc.* **2018**, *140*, 4678–4683.

(9) Jäger, M. O.; Morooka, E. V.; Federici Canova, F.; Himanen, L.; Foster, A. S. Machine learning hydrogen adsorption on nanoclusters through structural descriptors. *Npj Comput. Mater.* **2018**, *4*, 37.

(10) Holmberg, N.; Laasonen, K. Ab initio electrochemistry: Exploring the hydrogen evolution reaction on carbon nanotubes. *J. Phys. Chem. C* **2015**, *119*, 16166–16178.

(11) Skúlason, E.; Tripkovic, V.; Björketun, M. E.; Gudmundsdóttir, S.; Karlberg, G.; Rossmeisl, J.; Bligaard, T.; Jónsson, H.; Nørskov, J. K. Modeling the electrochemical hydrogen oxidation and evolution reactions on the basis of density functional theory calculations. *J. Phys. Chem. C* **2010**, *114*, 18182–18197.

(12) Van den Bossche, M.; Skúlason, E.; Rose-Petruck, C.; Jónsson, H. Assessment of constant-potential implicit solvation calculations of electrochemical energy barriers for H₂ evolution on Pt. *J. Phys. Chem. C* **2019**, *123*, 4116–4124.

(13) Lindgren, P.; Kastlunger, G.; Peterson, A. A. A challenge to the $G \sim 0$ interpretation of hydrogen evolution. *ACS Catal.* **2020**, *10*, 121–128.

(14) Kronberg, R.; Lappalainen, H.; Laasonen, K. Revisiting the Volmer-Heyrovský mechanism of hydrogen evolution on a nitrogen doped carbon nanotube: constrained molecular dynamics versus the nudged elastic band method. *Phys. Chem. Chem. Phys.* **2020**, *22*, 10536–10549.

(15) Henkelman, G.; Jónsson, H. Improved tangent estimate in the nudged elastic band method for finding minimum energy paths and saddle points. *J. Chem. Phys.* **2000**, *113*, 9978–9985.

(16) Henkelman, G.; Uberuaga, B. P.; Jónsson, H. A climbing image nudged elastic band method for finding saddle points and minimum energy paths. *J. Chem. Phys.* **2000**, *113*, 9901–9904.

(17) Sprik, M. Coordination numbers as reaction coordinates in constrained molecular dynamics. *Faraday Discuss.* **1998**, *110*, 437–445.

(18) Sakong, S.; Groß, A. The electric double layer at metal-water interfaces revisited based on a charge polarization scheme. *J. Chem. Phys.* **2018**, *149*, 084705.

(19) Kronberg, R.; Laasonen, K. Coupling surface coverage and electrostatic effects on the interfacial adlayer-water structure of hydrogenated single-crystal platinum electrodes. *J. Phys. Chem. C* **2020**, *124*, 13706–13714.

(20) Roman, T.; Groß, A. Structure of water layers on hydrogen-covered Pt electrodes. *Catal. Today* **2013**, *202*, 183–190.

(21) Sakong, S.; Forster-Tonigold, K.; Groß, A. The structure of water at a Pt(111) electrode and the potential of zero charge studied from first principles. *J. Chem. Phys.* **2016**, *144*, 194701.

(22) Le, J.; Iannuzzi, M.; Cuesta, A.; Cheng, J. Determining potentials of zero charge of metal electrodes versus the standard hydrogen electrode from density-functional-theory-based molecular dynamics. *Phys. Rev. Lett.* **2017**, *119*, 016801.

(23) Le, J.; Cuesta, A.; Cheng, J. The structure of metal-water interface at the potential of zero charge from density functional

theory-based molecular dynamics. *J. Electroanal. Chem.* **2018**, *819*, 87–94.

(24) Bouzid, A.; Pasquarello, A. Atomic-scale simulation of electrochemical processes at electrode/water interfaces under referenced bias potential. *J. Phys. Chem. Lett.* **2018**, *9*, 1880–1884.

(25) Sakong, S.; Gross, A. Water structures on a Pt(111) electrode from ab initio molecular dynamic simulations for a variety of electrochemical conditions. *Phys. Chem. Chem. Phys.* **2020**, *22*, 10431.

(26) Skúlason, E.; Karlberg, G. S.; Rossmeisl, J.; Bligaard, T.; Greeley, J.; Jónsson, H.; Nørskov, J. K. Density functional theory calculations for the hydrogen evolution reaction in an electrochemical double layer on the Pt(111) electrode. *Phys. Chem. Chem. Phys.* **2007**, *9*, 3241–3250.

(27) Marković, N. M.; Grgur, B. N.; Ross, P. N. Temperature-dependent hydrogen electrochemistry on platinum low-index single-crystal surfaces in acid solutions. *J. Phys. Chem. B* **1997**, *101*, 5405–5413.

(28) He, Z.-D.; Wei, J.; Chen, Y.-X.; Santos, E.; Schmickler, W. Hydrogen evolution at Pt(111)-activation energy, frequency factor and hydrogen repulsion. *Electrochim. Acta* **2017**, *255*, 391–395.

(29) Exner, K. S.; Sohrabnejad-Eskan, I.; Over, H. A universal approach to determine the free energy diagram of an electrocatalytic reaction. *ACS Catal.* **2018**, *8*, 1864–1879.

(30) Doering, D. L.; Madey, T. E. The adsorption of water on clean and oxygen-dosed Ru(011). *Surf. Sci.* **1982**, *123*, 305–337.

(31) Thiel, P. A.; Hoffmann, F. M.; Weinberg, W. H. Monolayer and multilayer adsorption of water on Ru(001). *J. Chem. Phys.* **1981**, *75*, 5556–5572.

(32) Sprik, M.; Ciccotti, G. Free energy from constrained molecular dynamics. *J. Chem. Phys.* **1998**, *109*, 7737–7744.

(33) Meijer, E. J.; Sprik, M. Ab initio molecular dynamics study of the reaction of water with formaldehyde in sulfuric acid solution. *J. Am. Chem. Soc.* **1998**, *120*, 6345–6355.

(34) Branduardi, D.; Gervasio, F. L.; Parrinello, M. From A to B in free energy space. *J. Chem. Phys.* **2007**, *126*, 054103.

(35) Tang, M. T.; Liu, X.; Ji, Y.; Nørskov, J. K.; Chan, K. Modeling hydrogen evolution reaction kinetics through explicit water-metal interfaces. *J. Phys. Chem. C* **2020**, *124*, 28083–28092.

(36) Fang, Y.-H.; Wei, G.-F.; Liu, Z.-P. Catalytic role of minority species and minority sites for electrochemical hydrogen evolution on metals: surface charging, coverage, and Tafel kinetics. *J. Phys. Chem. C* **2013**, *117*, 7669–7680.

(37) Marx, D.; Tuckerman, M. E.; Hutter, J.; Parrinello, M. The nature of the hydrated excess proton in water. *Nature* **1999**, *397*, 601.

(38) Filhol, J.-S.; Neurock, M. Elucidation of the electrochemical activation of water over Pd by first principles. *Angew. Chem., Int. Ed.* **2006**, *45*, 402–406.

(39) Taylor, C. D.; Wasileski, S. A.; Filhol, J.-S.; Neurock, M. First principles reaction modeling of the electrochemical interface: Consideration and calculation of a tunable surface potential from atomic and electronic structure. *Phys. Rev. B: Condens. Matter Mater. Phys.* **2006**, *73*, 165402.

(40) Chan, K.; Nørskov, J. K. Electrochemical barriers made simple. *J. Phys. Chem. Lett.* **2015**, *6*, 2663–2668.

(41) Chan, K.; Nørskov, J. K. Potential dependence of electrochemical barriers from ab initio calculations. *J. Phys. Chem. Lett.* **2016**, *7*, 1686–1690.

(42) Kastlunger, G.; Lindgren, P.; Peterson, A. A. Controlled-potential simulation of elementary electrochemical reactions: Proton discharge on metal surfaces. *J. Phys. Chem. C* **2018**, *122*, 12771–12781.

(43) Melander, M. M.; Kuisma, M. J.; Christensen, T. E. K.; Honkala, K. Grand-canonical approach to density functional theory of electrocatalytic systems: Thermodynamics of solid-liquid interfaces at constant ion and electrode potentials. *J. Chem. Phys.* **2019**, *150*, 041706.

(44) Melander, M. M. Grand canonical rate theory for electrochemical and electrocatalytic systems I: General formulation and

- proton-coupled electron transfer reactions. *J. Electrochem. Soc.* **2020**, *167*, 116518.
- (45) Komsa, H.-P.; Pasquarello, A. Finite-size supercell correction for charged defects at surfaces and interfaces. *Phys. Rev. Lett.* **2013**, *110*, 095505.
- (46) Fang, Y.-H.; Liu, Z.-P. Tafel kinetics of electrocatalytic reactions: from experiment to first-principles. *ACS Catal.* **2014**, *4*, 4364–4376.
- (47) Li, Q.; Ouyang, Y.; Lu, S.; Bai, X.; Zhang, Y.; Shi, L.; Ling, C.; Wang, J. Perspective on theoretical methods and modeling relating to electro-catalysis processes. *Chem. Commun.* **2020**, *56*, 9937–9949.
- (48) Bonnet, N.; Morishita, T.; Sugino, O.; Otani, M. First-principles molecular dynamics at a constant electrode potential. *Phys. Rev. Lett.* **2012**, *109*, 266101.
- (49) Bouzid, A.; Pasquarello, A. Redox Levels through Constant Fermi-Level ab Initio Molecular Dynamics. *J. Chem. Theory Comput.* **2017**, *13*, 1769–1777.
- (50) Haas, P.; Tran, F.; Blaha, P. Calculation of the lattice constant of solids with semilocal functionals. *Phys. Rev. B: Condens. Matter Mater. Phys.* **2009**, *79*, 085104.
- (51) Marković, N. M.; Ross, P. N. Surface science studies of model fuel cell electrocatalysts. *Surf. Sci. Rep.* **2002**, *45*, 117–229.
- (52) Conway, B. E.; Tilak, B. V. Interfacial processes involving electrocatalytic evolution and oxidation of H₂, and the role of chemisorbed H. *Electrochim. Acta* **2002**, *47*, 3571–3594.
- (53) Strmcnik, D.; Tripkovic, D.; Van der Vliet, D.; Stamenkovic, V.; Marković, N. Adsorption of hydrogen on Pt(111) and Pt(100) surfaces and its role in the HOR. *Electrochem. Commun.* **2008**, *10*, 1602–1605.
- (54) Schnur, S.; Groß, A. Challenges in the first-principles description of reactions in electrocatalysis. *Catal. Today* **2011**, *165*, 129–137.
- (55) Zhang, Q.; Liu, Y.; Chen, S. A DFT calculation study on the temperature-dependent hydrogen electrocatalysis on Pt(111) surface. *J. Electroanal. Chem.* **2013**, *688*, 158–164.
- (56) Lippert, G.; Hutter, J.; Parrinello, M. A hybrid Gaussian and plane wave density functional scheme. *Mol. Phys.* **1997**, *92*, 477–488.
- (57) Kühne, T. D.; Iannuzzi, M.; Del Ben, M.; Rybkin, V. V.; Seewald, P.; Stein, F.; Laino, T.; Khaliullin, R. Z.; Schütt, O.; Schiffmann, F.; et al. CP2K: An electronic structure and molecular dynamics software package-Quickstep: Efficient and accurate electronic structure calculations. *J. Chem. Phys.* **2020**, *152*, 194103.
- (58) Santarossa, G.; Vargas, A.; Iannuzzi, M.; Pignedoli, C. A.; Passerone, D.; Baiker, A. Modeling bulk and surface Pt using the "Gaussian and plane wave" density functional theory formalism: validation and comparison to k-point plane wave calculations. *J. Chem. Phys.* **2008**, *129*, 234703.
- (59) VandeVondele, J.; Hutter, J. Gaussian basis sets for accurate calculations on molecular systems in gas and condensed phases. *J. Chem. Phys.* **2007**, *127*, 114105.
- (60) Goedecker, S.; Teter, M.; Hutter, J. Separable dual-space Gaussian pseudopotentials. *Phys. Rev. B: Condens. Matter Mater. Phys.* **1996**, *54*, 1703.
- (61) Hartwigsen, C.; Goedecker, S.; Hutter, J. Relativistic separable dual-space Gaussian pseudopotentials from H to Rn. *Phys. Rev. B: Condens. Matter Mater. Phys.* **1998**, *58*, 3641.
- (62) Krack, M. Pseudopotentials for H to Kr optimized for gradient-corrected exchange-correlation functionals. *Theor. Chem. Acc.* **2005**, *114*, 145–152.
- (63) Hammer, B.; Hansen, L. B.; Nørskov, J. K. Improved adsorption energetics within density-functional theory using revised Perdew-Burke-Ernzerhof functionals. *Phys. Rev. B: Condens. Matter Mater. Phys.* **1999**, *59*, 7413.
- (64) Perdew, J. P.; Burke, K.; Ernzerhof, M. Generalized gradient approximation made simple. *Phys. Rev. Lett.* **1996**, *77*, 3865.
- (65) Grimme, S.; Antony, J.; Ehrlich, S.; Krieg, H. A consistent and accurate ab initio parametrization of density functional dispersion correction (DFT-D) for the 94 elements H-Pu. *J. Chem. Phys.* **2010**, *132*, 154104.
- (66) Mercurio, G.; McNellis, E. R.; Martin, I.; Hagen, S.; Leyssner, F.; Soubatch, S.; Meyer, J.; Wolf, M.; Tegeder, P.; Tautz, F. S.; et al. Structure and energetics of azobenzene on Ag(111): benchmarking semiempirical dispersion correction approaches. *Phys. Rev. Lett.* **2010**, *104*, 036102.
- (67) Klimeš, J.; Michaelides, A. Perspective: Advances and challenges in treating van der Waals dispersion forces in density functional theory. *J. Chem. Phys.* **2012**, *137*, 120901.
- (68) Marek, A.; Blum, V.; Johanni, R.; Havu, V.; Lang, B.; Auckenthaler, T.; Heinecke, A.; Bungartz, H.-J.; Lederer, H. The ELPA library: scalable parallel eigenvalue solutions for electronic structure theory and computational science. *J. Phys.: Condens. Matter* **2014**, *26*, 213201.
- (69) Bussi, G.; Donadio, D.; Parrinello, M. Canonical sampling through velocity rescaling. *J. Chem. Phys.* **2007**, *126*, 014101.
- (70) Ryckaert, J.-P.; Ciccotti, G.; Berendsen, H. J. Numerical integration of the cartesian equations of motion of a system with constraints: molecular dynamics of n-alkanes. *J. Comput. Phys.* **1977**, *23*, 327–341.
- (71) Trasatti, S. The absolute electrode potential: an explanatory note (Recommendations 1986). *Pure Appl. Chem.* **1986**, *58*, 955–966.
- (72) Bengtsson, L. Dipole correction for surface supercell calculations. *Phys. Rev. B: Condens. Matter Mater. Phys.* **1999**, *59*, 12301.
- (73) Fawcett, W. R. The ionic work function and its role in estimating absolute electrode potentials. *Langmuir* **2008**, *24*, 9868–9875.
- (74) Reiss, H.; Heller, A. The absolute potential of the standard hydrogen electrode: a new estimate. *J. Phys. Chem.* **1985**, *89*, 4207–4213.
- (75) Hansen, W.; Kolb, D. The work function of emersed electrodes. *J. Electroanal. Chem. Interfacial Electrochem.* **1979**, *100*, 493–500.
- (76) Kötz, E.; Neff, H.; Müller, K. A UPS, XPS and work function study of emersed silver, platinum and gold electrodes. *J. Electroanal. Chem. Interfacial Electrochem.* **1986**, *215*, 331–344.
- (77) Kelly, C. P.; Cramer, C. J.; Truhlar, D. G. Aqueous solvation free energies of ions and ion-water clusters based on an accurate value for the absolute aqueous solvation free energy of the proton. *J. Phys. Chem. B* **2006**, *110*, 16066–16081.
- (78) Donald, W. A.; Leib, R. D.; Demireva, M.; O'Brien, J. T.; Prell, J. S.; Williams, E. R. Directly relating reduction energies of gaseous Eu(H₂O)_n³⁺, n = 55–140, to aqueous solution: the absolute SHE potential and real proton solvation energy. *J. Am. Chem. Soc.* **2009**, *131*, 13328–13337.
- (79) Isse, A. A.; Gennaro, A. Absolute potential of the standard hydrogen electrode and the problem of interconversion of potentials in different solvents. *J. Phys. Chem. B* **2010**, *114*, 7894–7899.
- (80) Tripkovic, V.; Björketun, M. E.; Skúlason, E.; Rossmeisl, J. Standard hydrogen electrode and potential of zero charge in density functional calculations. *Phys. Rev. B: Condens. Matter Mater. Phys.* **2011**, *84*, 115452.
- (81) Hansen, M. H.; Rossmeisl, J. pH in grand canonical statistics of an electrochemical interface. *J. Phys. Chem. C* **2016**, *120*, 29135–29143.
- (82) Busch, M.; Laasonen, K.; Ahlberg, E. Method for the accurate prediction of electron transfer potentials using an effective absolute potential. *Phys. Chem. Chem. Phys.* **2020**, *22*, 25833–25840.
- (83) Manz, T. A.; Limas, N. G. Introducing DDEC6 atomic population analysis: part 1. Charge partitioning theory and methodology. *RSC Adv.* **2016**, *6*, 47771–47801.
- (84) Limas, N. G.; Manz, T. A. Introducing DDEC6 atomic population analysis: part 2. Computed results for a wide range of periodic and nonperiodic materials. *RSC Adv.* **2016**, *6*, 45727–45747.
- (85) Iyemperumal, S. K.; Deskins, N. A. Activation of CO₂ by supported Cu clusters. *Phys. Chem. Chem. Phys.* **2017**, *19*, 28788–28807.
- (86) Kubas, G. J. Fundamentals of H₂ binding and reactivity on transition metals underlying hydrogenase function and H₂ production and storage. *Chem. Rev.* **2007**, *107*, 4152–4205.

- (87) Gómez, R.; Orts, J. M.; Álvarez-Ruiz, B.; Feliu, J. M. Effect of temperature on hydrogen adsorption on Pt(111), Pt(110), and Pt(100) electrodes in 0.1 M HClO₄. *J. Phys. Chem. B* **2004**, *108*, 228–238.
- (88) Garcia-Araez, N.; Climent, V.; Feliu, J. M. Analysis of temperature effects on hydrogen and OH adsorption on Pt(111), Pt(100) and Pt(110) by means of Gibbs thermodynamics. *J. Electroanal. Chem.* **2010**, *649*, 69–82.
- (89) Yang, G.; Akhade, S. A.; Chen, X.; Liu, Y.; Lee, M.-S.; Glezakou, V.-A.; Rousseau, R.; Lercher, J. A. The nature of hydrogen adsorption on platinum in the aqueous phase. *Angew. Chem., Int. Ed.* **2019**, *58*, 3527–3532.
- (90) Chen, L. D.; Bajdich, M.; Martinez, J. M. P.; Krauter, C. M.; Gauthier, J. A.; Carter, E. A.; Luntz, A. C.; Chan, K.; Nørskov, J. K. Understanding the apparent fractional charge of protons in the aqueous electrochemical double layer. *Nat. Commun.* **2018**, *9*, 3202.
- (91) Marcus, R. A.; Sutin, N. Electron transfers in chemistry and biology. *Biochim. Biophys. Acta, Rev. Bioenerg.* **1985**, *811*, 265–322.
- (92) Hush, N. S. Electron transfer in retrospect and prospect: 1: Adiabatic electrode processes. *J. Electroanal. Chem.* **1999**, *460*, 5–29.
- (93) Exner, K. S. Does a thermoneutral electrocatalyst correspond to the apex of a volcano plot for a simple two-electron process? *Angew. Chem., Int. Ed.* **2020**, *59*, 10236–10240.
- (94) Exner, K. S. Hydrogen electrocatalysis revisited: Weak bonding of adsorbed hydrogen as design principle for active electrode materials. *Curr. Opin. Electrochem.* **2021**, *26*, 100673.
- (95) Nørskov, J. K.; Bligaard, T.; Logadottir, A.; Kitchin, J. R.; Chen, J. G.; Pandelov, S.; Stimming, U. Trends in the exchange current for hydrogen evolution. *J. Electrochem. Soc.* **2005**, *152*, J23–J26.
- (96) Ooka, H.; Nakamura, R. Shift of the optimum binding energy at higher rates of catalysis. *J. Phys. Chem. Lett.* **2019**, *10*, 6706–6713.
- (97) Dellago, C.; Bolhuis, P. G.; Chandler, D. On the calculation of reaction rate constants in the transition path ensemble. *J. Chem. Phys.* **1999**, *110*, 6617–6625.
- (98) Durst, J.; Simon, C.; Hasché, F.; Gasteiger, H. A. Hydrogen oxidation and evolution reaction kinetics on carbon supported Pt, Ir, Rh, and Pd electrocatalysts in acidic media. *J. Electrochem. Soc.* **2015**, *162*, F190.
- (99) Holmberg, N.; Laasonen, K. Diabatic model for electrochemical hydrogen evolution based on constrained DFT configuration interaction. *J. Chem. Phys.* **2018**, *149*, 104702.
- (100) Scheiber, H.; Shi, Y.; Khaliullin, R. Z. Communication: Compact orbitals enable low-cost linear-scaling ab initio molecular dynamics for weakly-interacting systems. *J. Chem. Phys.* **2018**, *148*, 231103.